

Flavor, transverse momentum, and azimuthal dependence of charged pion multiplicities in SIDIS with 10.6 GeV electrons

P. Bosted,¹ H. Bhatt,² S. Jia,³ W. Armstrong,⁴ D. Dutta,² R. Ent,⁵ D. Gaskell,⁵ E. Kinney,⁶ H. Mkrtchyan,⁷ S. Ali,⁸ R. Ambrose,⁹ D. Androic,¹⁰ C. Ayerbe Gayoso,² A. Bandari,¹ V. Berdnikov,⁸ D. Bhetuwal,² D. Biswas,¹¹ M. Boer,³ E. Brash,¹² A. Camsonne,⁵ M. Cardona,³ J. P. Chen,⁵ J. Chen,¹ M. Chen,¹³ E. M. Christy,¹¹ S. Covrig,⁵ S. Danagoulian,¹⁴ M. Diefenthaler,⁵ B. Duran,³ C. Elliot,¹⁵ H. Fenker,⁵ E. Fuchey,¹⁶ J. O. Hansen,⁵ F. Hauenstein,¹⁷ T. Horn,⁸ G. M. Huber,⁹ M. K. Jones,⁵ M. L. Kabir,² A. Karki,² B. Karki,¹⁸ S. J. D. Kay,^{9,19} C. Keppel,⁵ V. Kumar,⁹ N. Lashley-Colthirst,¹¹ W. B. Li,^{1,2} D. Mack,⁵ S. Malace,⁵ P. Markowitz,²⁰ M. McCaughan,⁵ E. McClellan,⁵ D. Meekins,⁵ R. Michaels,⁵ A. Mkrtchyan,⁷ C. Morean,^{15,5} G. Niculescu,²¹ I. Niculescu,²¹ B. Pandey,^{11,22} S. Park,²³ E. Pooser,⁵ B. Sawatzky,⁵ G. R. Smith,⁵ H. Szumila-Vance,^{5,20} A. S. Tadepalli,⁵ V. Tadevosyan,⁷ R. Trotta,⁸ H. Voskanyan,⁷ S. A. Wood,⁵ Z. Ye,^{4,24} C. Yero,²⁰ and X. Zheng¹³

(for the Hall C SIDIS Collaboration)

¹*The College of William & Mary, Williamsburg, Virginia 23185, USA*

²*Mississippi State University, Mississippi State, Mississippi 39762, USA*

³*Temple University, Philadelphia, Pennsylvania 19122, USA*

⁴*Argonne National Laboratory, Lemont, Illinois 60439, USA*

⁵*Thomas Jefferson National Accelerator Facility, Newport News, Virginia 23606, USA*

⁶*University of Colorado Boulder, Boulder, Colorado 80309, USA*

⁷*A.I. Alikhanyan National Science Laboratory,*

Yerevan Physics Institute, Yerevan 0036, Armenia

⁸*Catholic University of America, Washington, DC 20064, USA*

⁹*University of Regina, Regina, Saskatchewan S4S 0A2, Canada*

¹⁰*University of Zagreb, Zagreb, Croatia*

¹¹*Hampton University, Hampton, Virginia 23669, USA*

¹²*Christopher Newport University, Newport News, Virginia 23606, USA*

¹³*University of Virginia, Charlottesville, Virginia 22903, USA*

¹⁴*North Carolina A & T State University, Greensboro, North Carolina 27411, USA*

¹⁵*University of Tennessee, Knoxville, Tennessee 37996, USA*

¹⁶*University of Connecticut, Storrs, Connecticut 06269, USA*

¹⁷*Old Dominion University, Norfolk, Virginia 23529, USA*

¹⁸*Ohio University, Athens, Ohio 45701, USA*

¹⁹*University of York, Heslington, York, YO10 5DD, UK*

²⁰*Florida International University, University Park, Florida 33199, USA*

²¹*James Madison University, Harrisonburg, Virginia 22807, USA*

²²*Virginia Military Institute, Lexington, Virginia 24450, USA*

²³*Stony Brook University, Stony Brook, New York 11794, USA*

²⁴*Tsinghua University, Beijing 100084, China*

(Dated: December 30, 2025)

Abstract

Measurements of SIDIS multiplicities for π^+ and π^- from proton and deuteron targets are reported on a grid of hadron kinematic variables z , P_T , and ϕ^* for leptonic kinematic variables in the range $0.3 < x < 0.6$ and $3 < Q^2 < 5$ GeV 2 . Data were acquired in 2018-2019 at Jefferson Lab Hall C with a 10.6 GeV electron beam impinging on 10-cm-long liquid hydrogen and deuterium targets. Scattered electrons and charged pions were detected in the HMS and SHMS spectrometers, respectively. The multiplicities were fitted for each bin in (x, Q^2, z, P_t) to extract the ϕ^* - independent M_0 and the azimuthal modulations $\langle \cos(\phi^*) \rangle$ and $\langle \cos(2\phi^*) \rangle$. The P_t -dependence of the M_0 results was found to be remarkably consistent for the four cases studied: $ep \rightarrow e\pi^+X$, $ep \rightarrow e\pi^-X$, $ed \rightarrow e\pi^+X$, $ed \rightarrow e\pi^-X$ over the range $0 < P_t < 0.4$ GeV, as were the multiplicities evaluated near $\phi^* = 180^\circ$ over the extended range $0 < P_t < 0.7$ GeV. The Gaussian widths of the P_t -dependence exhibit a quadratic increase with z . The $\cos(\phi^*)$ modulations were found to be consistent with zero for π^+ , in agreement with previous world data, while the π^- moments were, in many cases, significantly greater than zero. The $\cos(2\phi^*)$ modulations were found to be consistent with zero. The higher statistical precision of this dataset of about 20,000 individual multiplicity values, compared to previously published data, should allow improved determinations of quark transverse momentum distributions and higher twist contributions.

I. INTRODUCTION

Over the last five decades, semi-inclusive deep-inelastic (SIDIS) lepton-nucleon scattering ($lN \rightarrow l'hX$) has proven to be a key tool in building a more complete and accurate picture of the internal structure of the nucleon in terms of the partonic degrees of freedom of quantum chromodynamics (QCD). It has been instrumental in establishing that the collinear picture of the quark-parton model is incomplete. One of the most important advantages of SIDIS is the ability to measure the yield of hadrons (h) both in terms of the longitudinal momentum fraction z and the transverse momentum P_t (shown schematically in Fig. 1). The SIDIS process in its simplest interpretation can be thought of as a subset of deep-inelastic scattering (DIS), described by parton distribution functions (PDFs), with a multiplicity function (M) that indicates the probability of the DIS final-state containing a particular meson with a particular momentum vector. In this highly simplified picture, the multiplicity dependence on P_t arises from a convolution of the transverse momentum of the quark (k_T) and the transverse momentum generated in the fragmentation process (p_\perp), in which the struck quark hadronizes into multiple final-state particles. A comparison of SIDIS from protons (u -quark dominated) and neutrons (d -quark dominated) could, in principle, be used to constrain the difference between the average k_T of up and down valence quarks in the nucleon. Expanding the kinematic coverage for both positive and negative pions can help to distinguish differences in “favored” and “unfavored” fragmentation functions, where “favored” refers to a pion containing the struck quark. The azimuthal modulations of the measured pion relative to the virtual photon direction are also sensitive to k_T , especially when the incident electron or the target nucleon are polarized. [1, 2]

In this paper, we present the results of a dedicated experiment at Jefferson Lab (JLab), designed to augment the global SIDIS dataset through high precision measurements from both hydrogen and deuteron targets, with measurements of both positively and negatively charged pions in the kinematic region accessible with a 10.6 GeV electron beam and in-plane spectrometers. The high luminosity of this experiment has permitted binning the multiplicity results in a fine three-dimensional grid in z , P_t , and azimuthal angle ϕ^* . Neither the beam nor the target was polarized for this experiment. Nevertheless, our results provide a crucial benchmark, at this energy, for the interpretation of SIDIS experiments with polarization degrees of freedom.

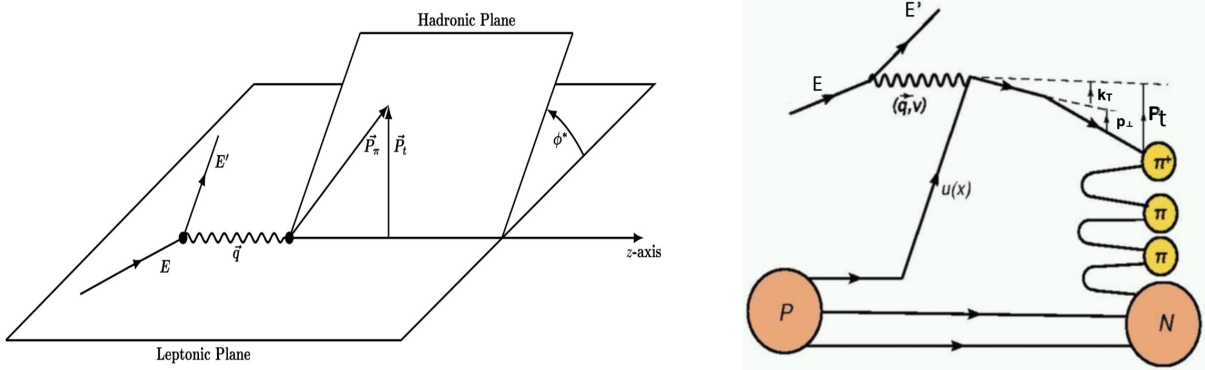


FIG. 1. (left) Kinematics of the SIDIS process in the γ^*P center of mass frame. (right) Simplified schematic of the pion SIDIS process, showing that the final transverse momentum of the leading pion, P_t , arises from the convolution of the struck quark's transverse momentum, k_T , with the transverse momentum generated during the fragmentation, p_\perp .

A. Formalism

The semi-inclusive scattering of unpolarized electrons by unpolarized nucleons in the SIDIS kinematic region can be described formally [3] in terms of structure functions (SF) as

$$\frac{d\sigma}{dx dy d\psi dz d\phi^* dP_t^2} = \frac{\alpha^2}{xyQ^2} \frac{y^2}{2(1-\epsilon)} \left(1 + \frac{\gamma^2}{2x}\right) \left\{ F_{UU,T} + \epsilon F_{UU,L} + \sqrt{2\epsilon(1+\epsilon)} \cos(\phi^*) F_{UU}^{\cos(\phi^*)} + \epsilon \cos(2\phi^*) F_{UU}^{\cos(2\phi^*)} \right\} \quad (1)$$

The four SF ($F_{UU,T}$, $F_{UU,L}$, $F_{UU}^{\cos(\phi^*)}$, and $F_{UU}^{\cos(2\phi^*)}$) are all functions of (x, Q^2, z, P_t) ; (x, Q^2, y) are the standard DIS virtual photon variables, ϵ is the virtual photon polarization, and the detected hadron is characterized by its momentum fraction z , transverse momentum P_t , and azimuthal angle ϕ^* of the hadronic reaction plane relative to the plane defined by the incident and scattered electron. We use the ‘‘Trento’’ convention for the definition of ϕ^* [3]. The fine structure constant is represented by α and the kinematic factor $\gamma = 2Mx/Q$, where M is the nucleon mass. We define multiplicities as the ratio of the SIDIS cross section (Eq. 1) to the DIS cross section, calculated as a function of (x, Q^2, y, ϵ) .

B. Theoretical interpretation

Although the intrinsic transverse momentum of the partons, \vec{k}_T , was already considered by Feynman when he introduced the parton model [4], the initial experimental and theoretical focus was on the one-dimensional light-cone momentum variable x . In recent years significant advances have been made in incorporating \vec{k}_T into the theoretical description of SIDIS processes. For example, the transverse momentum dependent (TMD) parton distribution functions (PDF) and fragmentation functions (FF) [5, 6] were introduced, and a TMD factorization formalism [7] was developed. The factorization framework demonstrates that the hadron transverse momentum arises from the transverse momentum of the quarks in the nucleon, convoluted with the transverse momentum generated during quark fragmentation. Both the TMD PDF and the FF depend on two independent variables: the TMD on x and k_T , while the FF depends on z and the transverse momentum p_\perp of the hadron acquired during the fragmentation process. The TMD factorization was first shown for the high-energy limit (high values of the virtuality scale, $Q^2 \gg \Lambda_{\text{QCD}}$) and moderate values of $P_t \sim \Lambda_{\text{QCD}}$. However, its applicability at moderate Q^2 (2 - 4 GeV 2) has since been observed in several experiments [8–11]. Within this framework, and with the approximation that higher-order (higher-twist) corrections are suppressed by powers of $1/Q$, the SIDIS differential cross section for polarized leptons on polarized nucleons is expressed in terms of 18 structure functions that are convolutions of various TMD PDF and FF [3]. This large number of structure functions is a consequence of the fact that, for a spin-1/2 hadron, there are 8 TMD [3, 5, 12], each representing a unique correlation between the spin and the orbital motion of the partons. These TMD are parameterized using the world data on SIDIS and other processes [13–17].

As expected, the unpolarized SIDIS cross section can only provide information about the unpolarized TMD distribution functions and the unpolarized TMD fragmentation functions. The $\cos(\phi^*)$ dependence was predicted in 1978 by R. Cahn [18] as a result of the interaction of the virtual photon with quarks in the nucleon possessing intrinsic transverse momentum. Both the $\cos(\phi^*)$ and $\cos(2\phi^*)$ modulations receive contributions from the Boer-Mulders effect [19], arising from a correlation between the quark's intrinsic transverse momentum and its transverse spin, coupled to the Collins fragmentation function [20], which preserves the correlation with fragmentation dependent on the struck quark's transverse spin. Phe-

nomenological analyses by Barone et al. [16] stress that these structure functions are sensitive to higher-twist contributions. Additionally, the transverse momentum dependence of the TMD and FF are expected to be approximately Gaussian [1], for low values of P_t . To leading order, this simplification and momentum conservation give: $\langle \vec{P}_t^2 \rangle \simeq \langle \vec{p}_\perp^2 \rangle + z^2 \langle \vec{k}_T^2 \rangle$, implying that the transverse momentum dependence of TMD and FF can be parameterized by a normalized linear combination of a Gaussian and a z^2 -weighted Gaussian [17]. This interpretation relies on $\langle \vec{p}_\perp^2 \rangle$ being independent of z , which is manifestly incorrect as $z \rightarrow 0$ at finite values of ν .

C. Previous experiments

Some of the earliest SIDIS experimental studies in the valence quark region ($x > 0.25$) were made at Cornell in the 1970s, using 12 GeV electrons [21], with an integrated luminosity several orders of magnitude lower than the present experiment with 10.6 GeV electrons. These experiments demonstrated that multiplicities behave roughly as $(1 - z)^2$ for $z < 0.7$, have an approximately Gaussian distribution in P_t , and have relatively small dependence on ϕ^* compared to exclusive pion electroproduction. Subsequent experiments by the HERMES collaboration [22, 23] used 27 GeV electrons or positrons scattering from very thin targets at DESY. The results are displayed as a function of z averaged over (x, Q^2, P_t) and a function of P_t averaged over (x, Q^2, z) , although a later publication [16] displays azimuthal asymmetries averaged over z in some bins in (x, Q^2) . The HERMES results are all at a bit higher values of W than the present experiment.

Experiments at CERN by the EMC [24] and later by the COMPASS collaboration [25, 26] collaboration used 100-200 GeV muon beams and focused on the sea quark region ($x < 0.3$). The most recent COMPASS publications show multiplicities as a function of z averaged over P_t [25], and azimuthal dependencies as a function of P_t averaged over x and z [27]. Earlier publications [26] are for un-separated hadrons from a nuclear target (LiD). All of the CERN results are at considerably higher values of W than the present experiment.

Global fits to the HERMES and COMPASS multiplicity results have shown that spin-averaged cross sections can be reasonably well described as a convolution of quark PDFs derived from DIS and Drell-Yan reactions with fragmentation functions (FF) derived from electron-positron colliders. They also demonstrated the usefulness of describing the produc-

tion of the leading meson that contains the struck quark flavor with “favored” FF, while other mesons are described by “unfavored” FF, which exhibit a smaller strength at high z than favored FF. In this paper, we compare our multiplicity results to a very recent global fits to the HERMES and COMPASS multiplicity results by the MAP collaboration [28], and to the azimuthal asymmetries by Barone et al. [16].

Jefferson Lab (JLab) offers the opportunity to perform much high luminosity SIDIS experiments, due to beam currents of up to $70 \mu\text{A}$, and an effective duty factor of 100%. A pilot experiment at JLab Hall C with 5.5 GeV electrons [8] showed an approximate duality between the results overlapping the traditional nucleon resonance region, at low center-of-mass energy ($2 < W < 2.6 \text{ GeV}$), and the results well above the nucleon resonance region ($W > 3 \text{ GeV}$). This was the case as long as the electron-pion invariant missing mass squared, M_x^2 , was well above 2.5 GeV^2 (corresponding to $z < 0.7$ at these kinematic settings). A noticeable peak centered at $M_x^2 = 1.5 \text{ GeV}^2$ is likely due to the semi-exclusive channel $ep \rightarrow e\pi\Delta(1232)$, which was not subtracted in that analysis (but is subtracted in the present analysis). Simple phenomenological fits [9, 11] to these data attempted to disentangle the up and down valence quark k_T widths, as well as favored and unfavored FF widths, with the assumptions that the $\cos(\phi^*)$ dependence is dominated by the Cahn term and that the fragmentation widths are independent of z (both of which have since been shown to be incorrect). Another JLab experiment using 5.5 GeV electrons was performed using the low beam currents and large acceptance CLAS detector [10]. Most of the results are at relatively low x and Q^2 , where counting rates are the highest. The results are shown as a function of z averaged over P_t .

II. THE EXPERIMENT

The experimental results prior to 2018 cannot be considered conclusive in the quark valence region ($x > 0.25$) due to the limited kinematic coverage, low counting rates, inadequate particle identification, and poor resolution in ϕ^* at low P_T . In order to overcome many of these limitations, a new experimental program was initiated in 2018 using beam energies up to 11 GeV with both the wide-acceptance, lower luminosity CLAS12 detector in Hall B and the high-luminosity, small acceptance spectrometers in Hall C. The broad program includes the use of beam and target polarization, both light and heavy nuclear targets, a

range of electron beam energies, and identification of many final-state mesons. In this paper, we report on spectrometer-based results for charged pions with an unpolarized target at the highest available beam energy, from an experiment that was an integral part of the JLab SIDIS program and was completed in 2019. The experiment featured a wide range of (x, Q^2) values (to study higher-twist contributions), full ϕ^* coverage for $P_t < 0.3$ GeV, a larger P_t range for ϕ^* near 180° , and a broad range in z (to help distinguish k_T width from p_\perp widths). The multiplicity results were published as a function of W integrated over ϕ^* and $0 < P_t < 0.2$ GeV in a recent Letter [29]. In this paper, we present results in a fully 3-dimensional grid in (z, P_t, ϕ^*) for three values of (x, Q^2) , spanning $2.6 < W < 3.3$ GeV.

The experiment was carried out in spring 2018 and fall 2019, in Hall C at JLab. Electrons scattered from hydrogen and deuterium cryogenic targets were detected in the High Momentum Spectrometer (HMS), with alternatively positive and negative pions detected in the Super High Momentum Spectrometer (SHMS). Additional details about the experiment can be found in Refs. [29, 30]. An overview of the experiment layout is shown in Fig. 2.

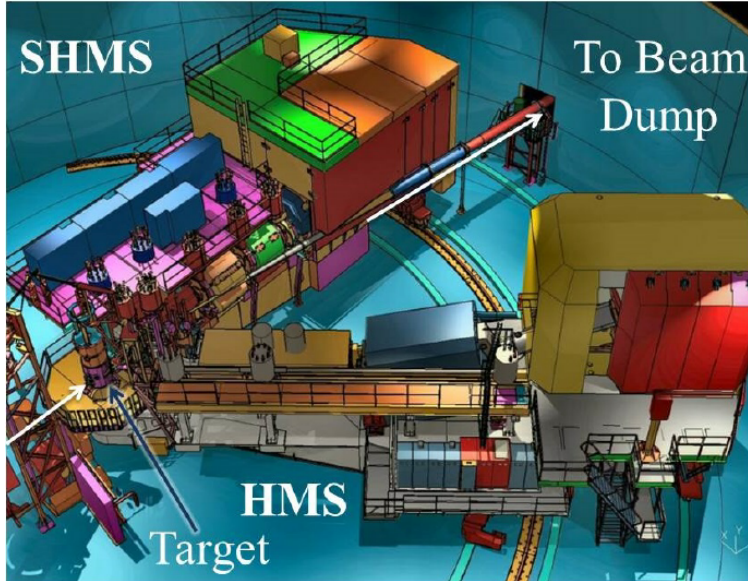


FIG. 2. Overview of the experimental setup in Hall C at JLab.

A. Electron beam

The experiment used a quasi-continuous-wave electron beam with beam energy of 10.6 GeV and beam currents ranging from $2 \mu\text{A}$ to $70 \mu\text{A}$. The spacing of the beam

micro-bunches was 4 ns for this experiment, and the beam was rastered over a 2×2 mm² square pattern at ≈ 25 kHz. The beam energy was determined with a relative uncertainty of $<0.05\%$. A set of resonant-cavity-based beam-current monitors (BCM) was used to determine the total accumulated beam charge with a relative uncertainty of $\approx 0.5\%$.

B. Targets

The two main production targets were liquid hydrogen and liquid deuterium, each circulated through 10 cm long and 3.4 cm radius aluminum cylinders. At the pressure and temperature used in the experiment, the nominal areal density of the LH₂ was 714 ± 14 mg/cm² for kinematic settings I and III, and 718 ± 8 mg/cm² for kinematic setting II (the kinematic settings are listed in Table I). The nominal areal density of the LD₂ was 1662 ± 33 mg/cm² for kinematic settings I and III, and 1662 ± 17 mg/cm² for kinematic setting II. A small reduction in the nominal density of the cryogenic targets due to beam heating was measured to be $-0.023\%/\mu\text{A}$. A so-called “dummy target” consisting of two aluminum foils each with an areal density of 181 mg/cm² placed 10 cm apart was used to measure the contribution from the entrance and exit end-caps of the cryogenic target cells. The targets were cycled every few hours, reducing the systematic errors on the ratio of multiplicities from hydrogen and deuterium, compared to experiments in which targets are changed on a much longer time frame.

TABLE I. Beam energy E , HMS momentum E' , HMS angle θ_e , corresponding values of DIS variables x , Q^2 , and W , and SHMS range of central momentum (p_π) and angle (θ_π) settings.

Setting	E	E'	θ_e	Q^2	W	x	p_π	θ_π	run-period
	(GeV)	(GeV)	(deg)	(GeV ²)	(GeV)		(GeV)	(deg)	
I	10.6	5.240	13.50	3.1	2.8	0.31	2.4 - 4.9	6.5 - 30	Spring 2018
II	10.6	3.307	19.70	4.1	3.3	0.30	2.6 - 6.6	6.5 - 22	Spring 2018
III	10.6	5.240	16.30	4.5	2.6	0.45	2.0 - 4.8	8 - 30	Fall 2019

C. Kinematics

The angle and momentum of the electron arm ($13^\circ < \theta_e < 20^\circ$, $3 < E' < 5.2$ GeV) and the hadron arm ($6^\circ < \theta_\pi < 30^\circ$, $2 < P_\pi < 6$ GeV) were chosen to map a region in x and z between 0.25-0.65 and 0.3-0.7, respectively. The spectrometers are constrained to rotate around the target in a horizontal plane, which limits the out-of-plane angular coverage to about 0.08 radians. The angle, θ_{pq} , between the electron three-momentum transfer, \vec{q} , and the hadron momentum was chosen to cover a range in P_t up to 0.8 GeV. The electron kinematic settings of the experiment are listed in Table I, along with the range of pion momenta and angles covered at each setting.

D. Electron identification

Scattered electrons were detected in the well-studied High Momentum Spectrometer [31], which has been in use since 1996.

Two drift chambers, each containing six planes of wires provided position and direction (track) information at the spectrometer focal plane with a resolution of $< 250 \mu\text{m}$. The track information was then used to reconstruct the momentum and angle of the particle at the target.

A two-mirror threshold gas Cherenkov detector and a segmented Pb-glass calorimeter [32] were used to distinguish electrons from pions (both of which generally passed the cut on scintillator paddles). The Cherenkov detector gas mixture and pressure were set to give a pion momentum threshold of 4.5 GeV. Detection efficiency was determined to be $> 99.5\%$ for settings I and II. For setting III, the average efficiency was 97.5% for the electrons, independent of beam current.

Scattered electrons were identified in the segmented lead glass electromagnetic calorimeter using the ratio of energy deposited in the blocks near the projected track position (E_{cal}) to the track momentum (P_e). As illustrated in Fig. 3, the E_{cal}/P_e distributions for each of the three kinematic settings show a narrow peak centered on unity. The vertical dashed line at 0.75 shows the cut used for electron identification. The electron detection efficiency of the HMS calorimeter was greater than 99.7%. After correcting for accidental coincidences, the contamination of pions in the final event sample was less than 0.5%.

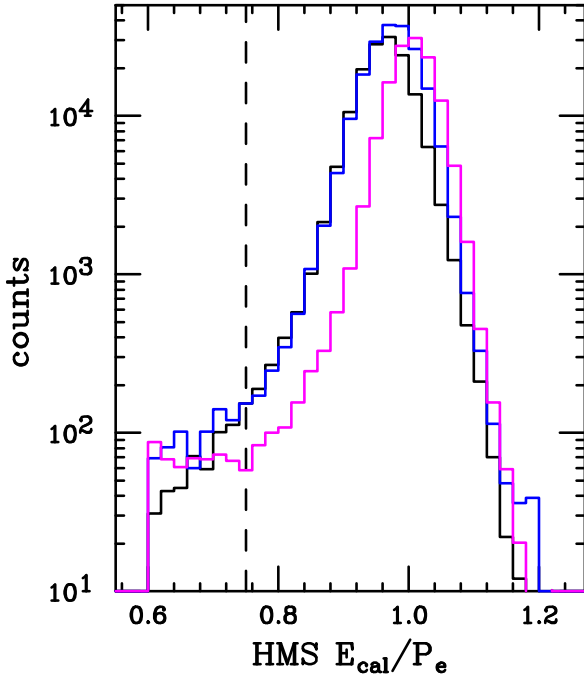


FIG. 3. Accidental-subtracted distributions of normalized HMS calorimeter energy (E_{cal}/p_e) for kinematic setting I (black), II (blue), and III (magenta), for electron-pion coincidence events passing all cuts except the $E_{cal}/p_e > 0.75$ cut, which is indicated by the vertical dashed line.

E. Pion identification

Charged pions were detected in the Super High Momentum Spectrometer [30], used for the first time in 2018. The momentum and angle ranges used at each kinematic setting are listed in Table I, and were chosen to provide good coverage in the region $0.3 < z < 0.7$, along with as much coverage in P_t and ϕ^* as allowed by the spectrometer constraints. The polarity of the spectrometer was alternated every few days in order to separately accumulate positively and negatively charged pions. This technique provides identical acceptance for both charge states, resulting in small systematic errors in the ratios of multiplicities, compared to large acceptance devices such as CLAS [33, 34].

As in the HMS, the SHMS detector configuration included two pairs of segmented hodoscope planes (three scintillator planes and one quartz plane) separated by 2 m to provide fast timing signals and rough particle trajectories. The resolution in particle speed was sufficient to reject protons with momenta below 2 GeV. The average arrival time in the four

paddles was compared to the arrival time of the 4 ns spaced beam micro-bunches—dubbed as the radio-frequency (RF) time. With a flight path of 22.5 m in the SHMS spectrometer, and a relative timing cut of ± 0.7 ns, it was possible to remove all protons and most kaons from the event sample, as illustrated in Fig. 4. The efficiency of the timing cut was about 96% for setting III. The RF timing signal was not operational for Settings I and II.

Two drift chambers, similar to those in the HMS, were used for tracking. (The tracking efficiency was found to drop from about 99.5% at low rates to about 97% at the highest rates of particles entering the detector hut. To avoid pile-up effects in the tracking, the particle rate was kept below 700 kHz by lowering the beam current to values as low as $2 \mu A$.

To separate pions from electrons (or positrons), kaons, and protons, three detectors were used: an aerogel Cherenkov detector, a heavy gas Cherenkov detector, and an electromagnetic lead-glass calorimeter. The aerogel detector was outfitted with multiple blocks with an index of refraction of 1.015, corresponding to Cherenkov light thresholds of 0.9, 2.85, and 5.4 GeV for pions, kaons, and protons, respectively. Above threshold, an average of 10 p.e. was produced. Below the Cherenkov threshold, kaons and protons often produced a few p.e. through knock-on scattering, as shown in Fig. 4. Therefore, a minimum of 4 p.e. was required for pion identification, with a corresponding efficiency of 95%.

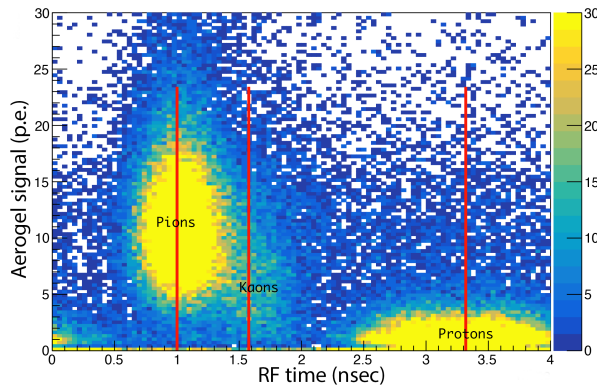


FIG. 4. SHMS aerogel signals (in p.e.) from setting III, as a function of the arrival time of pions, kaons, and protons relative to the beam micro-pulse time (RF time), modulo the 4 ns bunch spacing, for particles with momenta $3.4 < P_\pi < 4.3$ GeV. The pion arrival time was shifted such that its peak is at 1 ns. The red vertical lines show the location of the pion, kaon, and proton peaks.

The heavy gas Cherenkov detector contained $\text{C}_4\text{F}_8\text{O}$ at less than 1 atm pressure, giving a pion threshold of 2.61 GeV. It has a small inefficient region near the center of the detector for settings I and II, and a much larger region for setting III. Pions with momenta above 2.85 GeV were required to have tracks outside the inefficient region and a light signal greater than 1 p.e. The efficiency of this cut varied with momentum, increasing rapidly from 96% at 2.85 GeV to 99% for $P_\pi > 3.2$ GeV.

The segmented lead-glass, 22 radiation-length electromagnetic calorimeter was used to separate hadrons from electrons. In contrast to the HMS, where electrons produced a narrow peak in E_{cal}/P_e centered on unity, hadrons in the SHMS generally produced much less visible energy, as seen in the E_{cal}/P_π distribution, because the calorimeter is only about one hadronic interaction length in thickness. The distributions in E_{cal}/P_π are shown for both positive (top panel) and negative polarity (bottom panel) in Fig. 5, for good pion candidates selected by all cuts except that on E_{cal}/P_π . A peak near unity can be seen in the negative polarity distribution, which we ascribe to accidental electron-electron coincidences. The peak is largely suppressed when accidental coincidences are removed (blue curves). There is essentially no evidence of electron-positron coincidences in the positive polarity distributions. The residual distributions for $E_{\text{cal}}/P_\pi > 0.8$ are likely dominated by charged-to-neutral pion conversions at the start of the hadronic shower process. Nonetheless, we imposed a cut $E_{\text{cal}}/P_\pi < 0.8$ to ensure no electron or positron contamination of the pion signal, with a typical efficiency of 0.94-0.97, depending on the spectrometer momentum.

The noble gas Cherenkov detector was installed only for settings I and II. With a pion threshold of over 5 GeV, it was not directly used for pion identification. Its main use was to provide a clean sample of electrons for calibrating the calorimeter. Additional information on the detectors used in the experiment, plots of the trigger efficiency, and the detector efficiencies can be found in Ref. [29, 35, 36].

F. Electron-pion coincidence identification

At the high luminosity of Hall C, there were many triggers for which an electron and a pion originate from different beam bunches, spaced by 4 ns for this experiment. The average number of events in four accidental peaks (2 on either side of the true coincidence peak) was subtracted from the central peak to select true electron-pion coincidences. For settings I

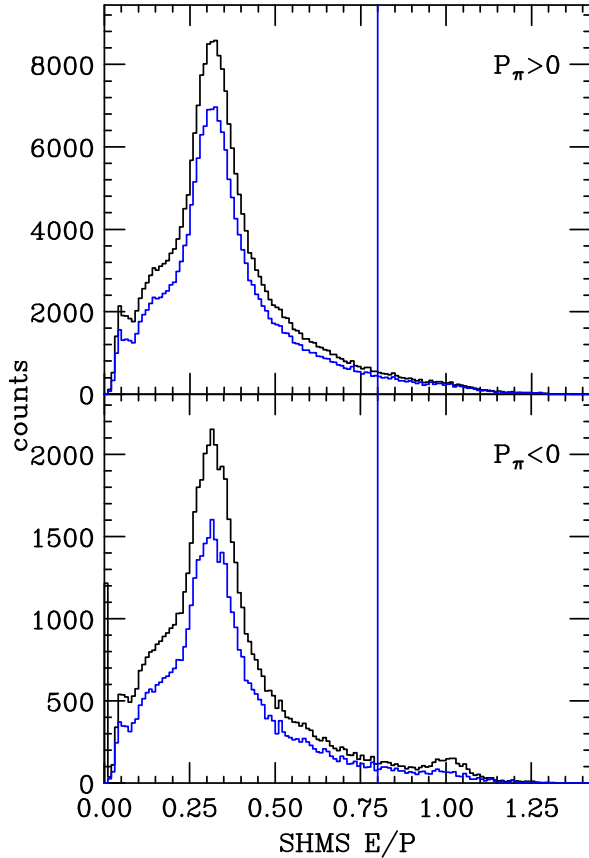


FIG. 5. Distributions of E_{cal}/P_π in the SHMS calorimeter for positive (top panel) and negative (bottom panel) pion candidates. The sign of P_π refers to the polarity of the spectrometer. The blue curves represent subsets of the black distributions with accidental coincidences subtracted. The vertical line at 0.8 indicates the cut used to reject positrons (top panel) and electrons (bottom panel).

and II (Spring 2018), the peak width was about 0.4 ns, consistent with the expected timing resolution of the trigger scintillators in both spectrometers, and a cut of ± 1 ns was used to identify in-time coincidences. For setting III (Fall 2018), a mis-cabling problem caused the peak to be much wider (2.2 ns), reducing the ability to reject kaons and protons using coincidence timing. A wider cut of ± 2 ns was therefore applied for setting III. Fortunately, the RF timing was operational for setting III, which more than compensated for this deficiency. The accidental-to-real ratio varied throughout the experiment from 10% to 50%.

G. Readout trigger and data acquisition

The trigger consisted of in-time signals on any three out of the four hodoscope planes in each spectrometer. This ensured essentially 100% trigger efficiency. The timing resolution of each plane was about 0.5 ns, resulting in an accuracy of typically 0.3 ns for the electron-pion time difference. The trigger signaled the Data Acquisition (DAQ) system [37] to read out pulse time and height information for all the detectors in both spectrometers, and record them at rates of up to 3000 Hz.

During the Spring 2018 runs (settings I and II), several problems caused a rate-dependent loss of information for the desired electron-pion coincidences. The multiplicative correction factor C_{DT} for these effects, determined by running with different beam currents under otherwise identical conditions, was parameterized as: $C_{DT} = 1.03 + 0.19(R_{HMS} + R_{SHMS})$ where R_{HMS} and R_{SHMS} are the trigger rates in the two spectrometers, in MHz. The factor of 1.03 at zero luminosity was obtained by comparing to Spring 2018 runs (setting III), for which most of the problems of settings I and II were fixed, and the luminosity correction is much smaller: $C_{DT} = 1 + 0.04(R_{HMS} + R_{SHMS})$.

H. Pair-symmetric background

In inclusive electron scattering, an important background process occurs when the measured electron originates from the decay of a final-state hadron, especially for low values of E'/E . Approximately equal contributions come from the Dalitz decay $\pi^0 \rightarrow \gamma e^+ e^-$ and from the dominant $\pi^0 \rightarrow \gamma\gamma$ decay, followed by subsequent pair production from one of the photons in the target or spectrometer entrance window. This so-called pair-symmetric background is greatly reduced in SIDIS compared to DIS by the requirement of a coincident pion at relatively large transverse momentum with respect to the electron beam. We performed a dedicated measurement of the pair-symmetric background by reversing the polarity of the HMS spectrometer and detecting the scattered positrons at two settings where the background was expected to be the largest. The results, tabulated in Table II, indicate that the pair-symmetric background is well below 0.5%.

We also measured the pair-symmetric background for all the momentum/angle settings of this experiment, by exchanging the roles of the two spectrometers. The ratios of these

TABLE II. Ratios of SIDIS rates with positrons compared to electrons in the HMS. The momentum of the HMS was 3.6 GeV and the angle was 19 degrees. Pions were measured in the SHMS with momenta of 2.6 GeV and angles of 16 and 20 degrees. The sign of P_p refers to the polarity of the spectrometer.

$P_p(GeV)$	$\theta_p(deg)$	target	e^+/e^-
-2.6	16	p	0.002 ± 0.002
		d	0.004 ± 0.002
	20	d	0.004 ± 0.002
		p	0.004 ± 0.004
+2.6	20	p	0.000 ± 0.002
		d	0.002 ± 0.001
	16	d	0.000 ± 0.001

450 measurements lie in the range 0 to 1%, with an average of about 0.3%.

Based on these results, we did not apply any pair-symmetric correction, but assigned a systematic uncertainty of 0.3% due to this omission.

III. MONTE CARLO SIMULATION

A Monte Carlo (MC) simulation [38], named SIMC, was performed for each target and pair of spectrometer settings primarily to model the spectrometer acceptance and evaluate radiative corrections. Another important use was to model pion and kaon decays (which led to muons and pions in the SHMS detector hut, respectively). For each setting, the simulation was used to generate a large number of events for three distinct physics processes: charged pion SIDIS itself (see Sec. III A); and the two background processes, exclusive pion production and the semi-exclusive $\pi\Delta(1232)$ final-state arising from bremsstrahlung emitted by either the incoming or the outgoing electron. These radiative contributions were treated in the angle peaking approximation using the formalism of Mo and Tsai [39]. The simulation also includes a detailed model of the targets, and geometrical acceptance and magnetic field map of the spectrometer magnets. The MC accounted for energy loss and multiple scattering in the target, vacuum windows, and detectors. Meson decays were allowed at any point along

the particle trajectory, with the charged decay products tracked through the remainder of the spectrometer. The MC has been demonstrated to accurately reproduce the performance of the Hall C spectrometers [35]. The multiplicity and cross section models used in the simulation are described in the next three sections. The SIDIS model was improved by scaling the ratio of measured yields to the MC yield and iterating this process.

A. SIDIS model

After two iterations, the charged pion SIDIS cross section model, obtained using a global fit to our results, augmented with world data is given by:

$$\sigma_{SIDIS} = \sigma_{DIS}(x, Q^2, \epsilon) M_{SIDIS}(z, P_t, \phi^*, x, Q^2). \quad (2)$$

The inclusive DIS cross section $\sigma_{DIS}(x, Q^2, \epsilon)$ is from a global fit to all world data available by the year 2020 for electrons scattering from both proton and deuteron targets [40]. It is the most comprehensive model of the DIS cross section measured with the electron spectrometer used in this experiment, and the inclusive data collected at the kinematic settings used in this paper were found to be consistent with this model to within a few percent.

The z -dependence of the multiplicity function $M_{SIDIS}(z, P_t, \phi^*, x, Q^2)$ is given by:

$$\begin{aligned} zM_{p\pi^+}(z, x, Q^2) &= (q_u^2 u D_f + q_u^2 \bar{u} D_u + q_d^2 d D_u + q_d^2 \bar{d} D_f + q_s^2 s D_u + q_s^2 \bar{s} D_u) / \sum (q_i)^2 \\ zM_{p\pi^-}(z, x, Q^2) &= (q_u^2 u D_u + q_u^2 \bar{u} D_f + q_d^2 d D_f + q_d^2 \bar{d} D_u + q_s^2 s D_u + q_s^2 \bar{s} D_u) / \sum (q_i)^2 \\ zM_{n\pi^+}(z, x, Q^2) &= (q_d^2 d D_f + q_u^2 \bar{d} D_u + q_d^2 u D_u + q_d^2 \bar{u} D_f + q_s^2 s D_u + q_s^2 \bar{s} D_u) / \sum (q_i)^2 \\ zM_{n\pi^-}(z, x, Q^2) &= (q_d^2 d D_u + q_u^2 \bar{d} D_f + q_d^2 u D_f + q_d^2 \bar{u} D_u + q_s^2 s D_u + q_s^2 \bar{s} D_u) / \sum (q_i)^2 \end{aligned} \quad (3)$$

where, $M_{p/n\pi^\pm}(z, x, Q^2)$ are the charged pion multiplicities from the proton (p) and neutron (n), q_i are the quark charges, the quark distribution functions $u, d, s, \bar{u}, \bar{d}, \bar{s}$ were taken from CTEQ5 [41], and the favored and unfavored fragmentation functions D_f and D_u were parameterized as:

$$D_{f/u} = p_1 \zeta^{(p_2 + p_4 s_v + p_9 W^{-1})} (1 - \zeta)^{(p_3 + p_5 s_v + p_{10} W^{-1})} (1 + p_6 \zeta + p_7 \zeta^2 + p_8 \zeta^3) (1 + p_{11} W^{-1} + p_{12} W^{-2}), \quad (4)$$

where, $s_v = \ln(Q^2/2)$ and the target mass corrections were applied using [42]

$$\zeta = z \frac{1 + \sqrt{1 - 4x^2(m_\pi^2 + P_t^2)/z^2 Q^2}}{1 + \sqrt{1 + 4x^2 M^2/Q^2}} \quad (5)$$

The fit parameters p_i were obtained from an iterative fit to the data of this experiment, and are given in Table III.

TABLE III. Table of parameters used for $D_{f/u}$.

	p_1	p_2	p_3	p_4	p_5	p_6	p_7	p_8	p_9	p_{10}	p_{11}	p_{12}
D_f	1.0424	-0.1714	1.8960	-0.0307	0.1636	-0.1272	-4.2093	5.0103	2.7406	-0.5778	0	3.5292
D_u	0.7840	0.2369	1.4238	0.1484	0.1518	-1.2923	-1.5710	3.0305	1.1995	1.3553	2.5868	8.0666

The P_t -dependence of the multiplicity functions was incorporated as:

$$M_{p/n\pi^\pm}(z, P_t, \phi^*, x, Q^2) = \frac{1}{2\pi} M_0(z, x, Q^2) b e^{-bP_t^2}, \quad (6)$$

i.e., a Gaussian distribution with the parameter $b = (0.12z^2 + 0.2)^{-1}$ GeV $^{-2}$, common to all processes with amplitude $M_0(z, x, Q^2)$. Note that we do not have any azimuthal dependence in this fit, consistent with the π^+ results of the present experiment. Also note that we do not have a factorized expression: the multiplicity function depends on the electron variables (x, Q^2, W) , which we found necessary to describe the data of this experiment.

B. Exclusive pion production model

The cross section for exclusive charged pion electroproduction is defined as:

$$\sigma = \frac{1.359}{(s - M^2)^2} (\sigma_T + \epsilon \sigma_L + \epsilon \cos(2\phi^*) \sigma_{TT} + \sqrt{2\epsilon(1+\epsilon)} \cos(\phi^*) \sigma_{LT}) \quad (7)$$

where all relevant units are in GeV, M is the average nucleon mass, and the longitudinal and transverse cross sections σ_L, σ_T , as well as two interference terms σ_{LT} and σ_{TT} are given in terms of the pion form factor F_π by:

$$\begin{aligned} F_\pi &= (1 + p_1 Q^2 + p_2 Q^4)^{-1} \\ \sigma_L &= (p_3 + p_{15}/Q^2) |t| / (|t| + 0.02)^2 Q^2 F_\pi^2 (s^{p_{11}} + \sqrt{s^{p_{17}}}) e^{p_4 |t|} \\ \sigma_T &= p_5 / Q^2 e^{p_6 Q^4} / (s^{p_{12}} + \sqrt{s^{p_{16}}}) e^{p_{14} |t|} \\ \sigma_{LT} &= (p_7 / (1 + p_{10} Q^2)) e^{p_8 |t|} \sin(\theta_{cm}) / s^{p_{13}} \\ \sigma_{TT} &= (p_9 / (1 + Q^2)) e^{-7.0 |t|} \sin(\theta_{cm})^2 \end{aligned} \quad (8)$$

The parameters p_i for exclusive pion production from the proton ($ep \rightarrow e\pi^+n$) and the neutron ($en \rightarrow e\pi^-p$) are obtained from fits to world data on LT separated pion electroproduction cross sections [43] and are shown in Tables IV and V.

TABLE IV. Table of parameters used for exclusive pion electroproduction cross sections.

	p_1	p_2	p_3	p_4	p_5	p_6	p_7	p_8	p_9	p_{10}
n_{π^-p}	1.60077	-0.01523	37.08142	-4.11060	23.26192	0.00983	0.87073	-5.77115	-271.08678	0.13766
p_{π^+n}	1.75169	0.11144	47.35877	-4.69434	1.60552	0.00800	0.44194	-2.29188	-41.67194	0.69475

TABLE V. Table of parameters used for exclusive pion electroproduction cross sections.

	p_{11}	p_{12}	p_{13}	p_{14}	p_{15}	p_{16}	p_{17}
n_{π^-p}	-0.00855	0.27885	-1.13212	-1.50415	-6.34766	0.55769	-0.01709
p_{π^+n}	0.02527	-0.50178	-1.22825	-1.16878	5.75825	-1.00355	0.05055

C. Model for $\pi\Delta$

We modeled the semi-exclusive reactions with $\pi\Delta(1232)$ in the final-state by simply scaling fully exclusive pion electroproduction by the effective Clebsch–Gordan coefficients determined from a fit to the data of this experiment. The coefficients are given by:

$$(ep \rightarrow e\pi^+\Delta^0)/(ep \rightarrow e\pi^+n) = 0.4$$

$$(en \rightarrow e\pi^+\Delta^-)/(ep \rightarrow e\pi^+n) = 0.8$$

$$(ep \rightarrow e\pi^-\Delta^{++})/(en \rightarrow e\pi^-p) = 0.55$$

$$(en \rightarrow e\pi^-\Delta^+)/(en \rightarrow e\pi^-p) = 1.0$$

The final-state missing mass was simulated using a Breit–Wigner distribution for the $\Delta(1232)$.

D. Kinematic dependence of radiative corrections

The P_t and z dependence of the radiative corrections follows a similar pattern, with the overall ratio decreasing at high P_t or z , resulting from a strong increase of the exclusive

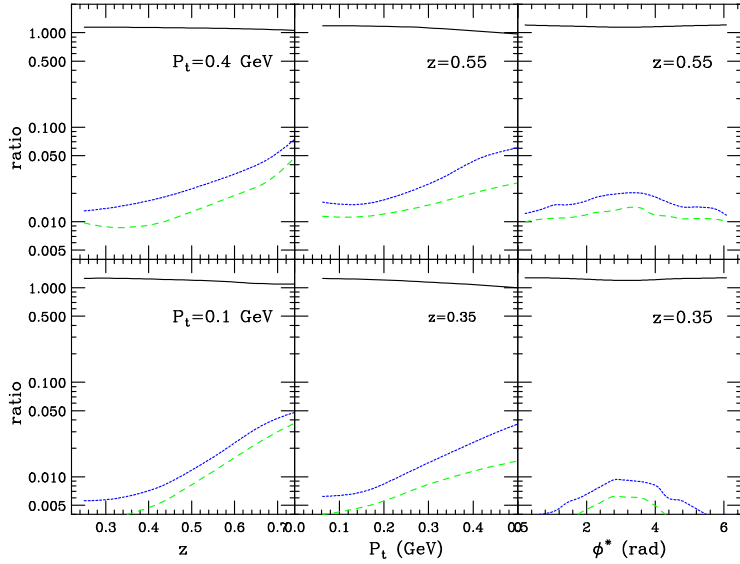


FIG. 6. The solid black curves illustrate the ratio of radiated cross sections to Born cross sections for π^+ from a deuteron target with $x = 0.3$ and $Q^2 = 3 \text{ GeV}^2$. They are plotted in the left-hand panels as a function of z at $\phi^* = 180^\circ$ for two values of P_t ; in the middle panels as a function of P_t for two values of z ; and in the right-hand panels as a function of ϕ^* for two values of z . The short-dashed blue curves show the relative contribution of the radiative tail from exclusive pion production, while the long-dashed green curves show the contributions from the $\pi\Delta$ radiative tail.

and $\pi\Delta$ contributions being more than offset by a depletion of SIDIS events, as illustrated in the middle panels of Fig. 6. The ϕ^* dependence of the radiative corrections indicates a small but non-negligible $\cos(\phi^*)$ dependence, with the exclusive pion and $\pi\Delta$ contributions peaking near 180° , as shown in the right-hand panels of Fig. 6.

The exclusive pion and $\pi\Delta$ corrections were assumed to be subtractive, and reduced the measured cross section by as much as 7% in the worst case. The multiplicative correction factor ranged from 0.8 at high z to 1.2 at low z .

E. Acceptance corrections

The predicted yields were corrected for small mismatches between the Monte Carlo simulation of the spectrometers and the actual acceptance. Three-dimensional grids in relative

momentum ($\frac{p-p_0}{p_0}$), where p_0 is the central momentum, and the Euler angles in the x and y directions (x'_{tar} —vertical, and y'_{tar} —pointing left) reconstructed to the frame of the target, were constructed by minimizing the χ^2 to achieve agreement among the data taken at different central momenta and scattering angles, using the entire dataset of this experiment. The multiplicative correction factors, shown in Fig. 7, are applied to the event-by-event weights for events generated in SIMC. For the HMS spectrometer, one of the prominent features is a “dip” near $\frac{p-p_0}{p_0} = -2\%$ for the central scattering angles, with only minor dependence on out-of-plane angle. This feature has been noted before in previous one-dimensional studies that only looked at the dependence on $\frac{p-p_0}{p_0}$. This new 3D study shows that the “dip” becomes more of a “bump” at larger absolute values of y'_{tar} , and also shows some non-trivial x'_{tar} dependence. The SHMS spectrometer was new for this experiment, so our acceptance study is the first one. We found little dependence on vertical angle in the region $-0.03 < x'_{tar} < 0.03$ rad, where the bulk of the data reside. We found a considerable $\frac{p-p_0}{p_0}$ dependence which itself is significantly dependent on scattering angle.

The SHMS and HMS momentum range used for this analysis was $-16\% < dp/p < +18\%$ and $-9\% < dp/p < +11\%$, respectively, for central angles. For extreme values of in-plane and out-of-plane angles, for which acceptance corrections were more than $\approx 10\%$ away from unity, more restrictive dp/p ranges were used. The SHMS and HMS in-plane relative angle range for this analysis was $-30 \text{ mr} < y'_{tar} < 30 \text{ mr}$, while the out of plane relative angle range was $-55 \text{ mr} < x'_{tar} < 55 \text{ mr}$ and $-65 \text{ mr} < x'_{tar} < 65 \text{ mr}$ respectively.

F. Event selection cuts and efficiency corrections

The SIMC weights were also corrected event-by-event for the detector efficiencies, which can vary with position in the spectrometer hut, especially for the heavy gas Cherenkov detector in the SHMS. The same event selection cuts were used on the SIMC track positions at the HMS and SHMS detectors, spectrometer exit apertures, and reconstructed momenta and angles as for the actual experimental data. An overall factor of 0.99 was applied to account for pion absorption in the target.

The quality of the models and corrections used in the simulation is demonstrated in Fig. 8, showing the good agreement between the experimental yields and simulated yields for setting I with the SHMS spectrometer centered on $z = 0.9$ to capture the contributions

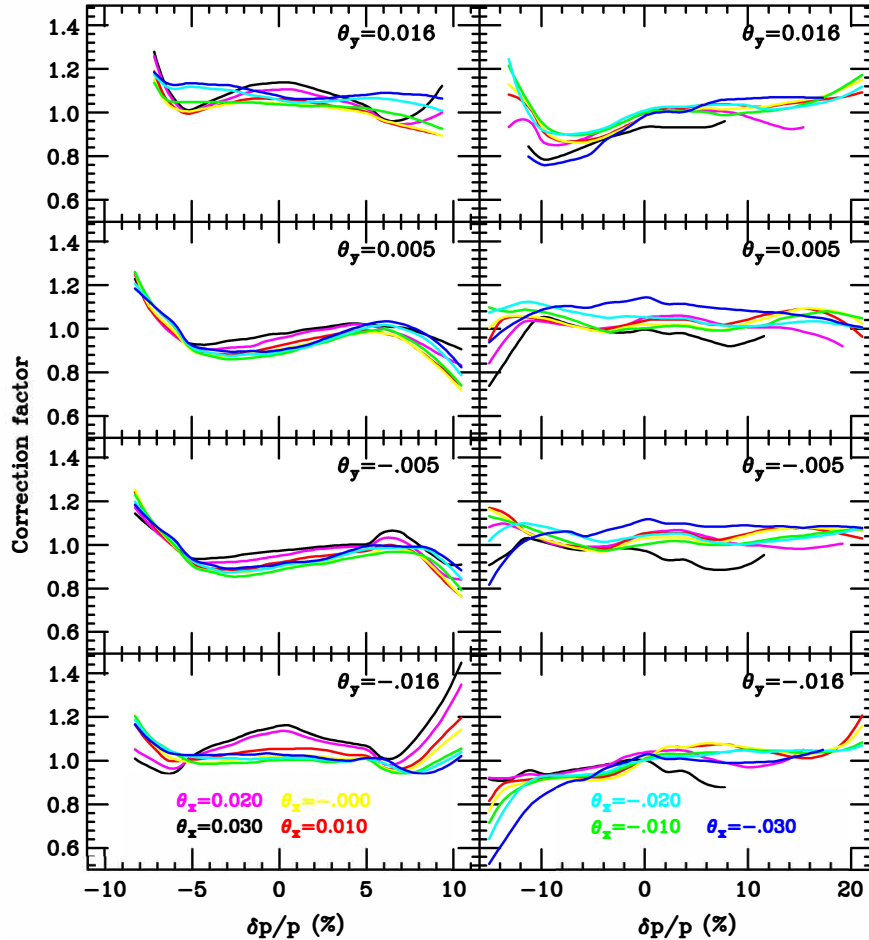


FIG. 7. Acceptance correction factors as a function of $\frac{p-p_0}{p_0}$ for four bins in in-plane relative scattering angle θ_y for HMS (left-hand column) and SHMS (right-hand column). The different colors correspond to bins in out-of-plane angle θ_x .

for exclusive pion production (centered on electron-pion missing mass $M_x = 0.94$ GeV), $\pi\Delta$ electroproduction (centered on $M_x = 1.232$ GeV), and high- z SIDIS from both the target liquid and endcap (“dummy target”).

IV. RESULTS

A. Data analysis

For each set of data with identical settings and target, the number of electron-pion coincidences, corrected for accidental and target endcap contributions, were divided by the

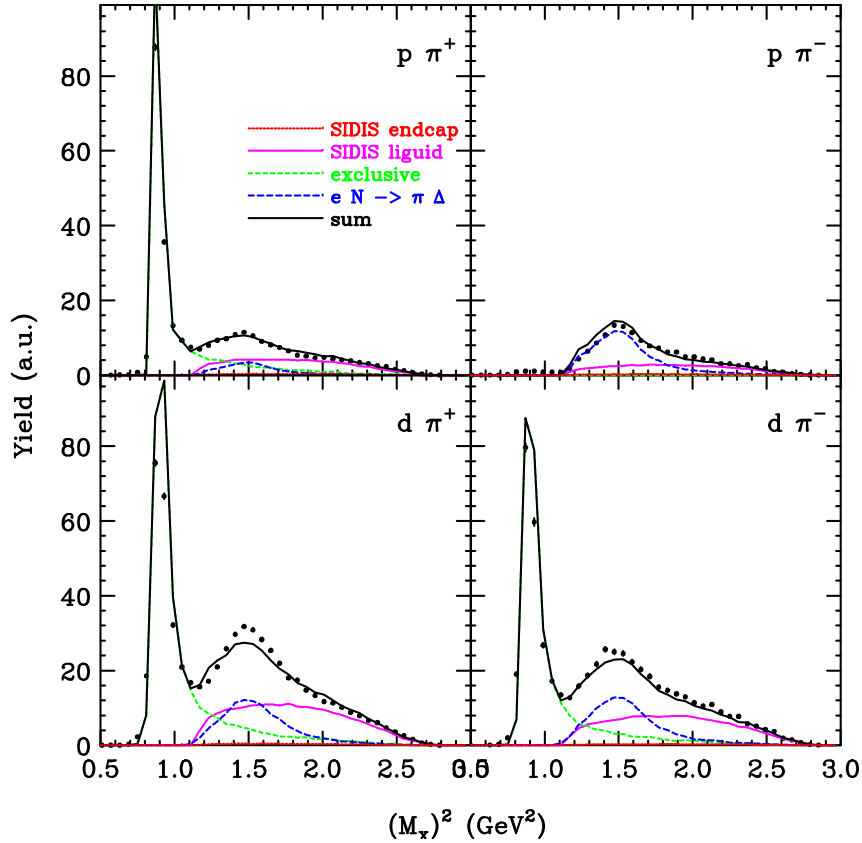


FIG. 8. Experimental yields as a function of electron-pion missing mass squared for setting I from auxiliary runs taken with the SHMS centered on $z = 0.9$, compared to the predicted Monte Carlo yields for SIDIS, exclusive pion production, and $\pi\Delta$ production. Results are shown for both π^+ (left panels) and π^- production (right panels) and proton (top row) and deuteron targets (bottom row). The statistical uncertainty of the data points are smaller than the size of the points.

accumulated beam charge to form an experimental yield Y_{exp} .

The corrected yields were binned in a three-dimensional grid with twenty bins in z from 0 to 1, 16 bins in P_t from 0 to 1, and 15 bins in ϕ^* from 0 to 2π . The predicted yields, Y_{MC} , from the MC simulation of each dataset were accumulated into the same kinematic grid as the experimental data. The simulated yields included contributions from SIDIS itself as well as the radiative tails from the exclusive pion and $\pi\Delta$ reactions. The predicted yields were corrected for all detector and PID efficiencies as well as the luminosity dependence. The same detector position, magnet aperture, and reconstructed track variables were used as for the experimental data.

Experimental multiplicities, defined as the ratio of the SIDIS cross section ($d\sigma_{ee'\pi X}$) to the inclusive DIS cross section ($d\sigma_{ee'X}$), were determined for each kinematic bin by:

$$M_i(z, P_t, \phi^*) = M_0(x, Q^2, z, P_t, \phi^*) \frac{Y_{exp}}{Y_{MC}} \quad (9)$$

for each target nucleus (p/d), HMS polarity, and (x, Q^2) HMS setting, where M_0 is the multiplicity model used in the MC simulation, evaluated at the center of each bin, and the index i covers the SHMS settings that provide overlap in (z, P_t, ϕ^*) . In most cases, there were two overlapping settings, but occasionally there were three or four overlaps. The final results were taken as the weighted average of all M_i that contribute to each bin.

The results discussed in this paper included the additional cut $M_x > 1.6$ GeV, to remove the region where contributions from nucleon resonances, semi-exclusive processes, and higher-twist effects appear to be large, as was found in Ref. [8]. This cut was removed in the version of the analysis used to iterate the SIDIS model used in the Monte Carlo simulation.

Numerical results for the multiplicities are tabulated in a full three-dimensional grid in (z, P_t, ϕ^*) for each target, pion polarity, and HMS setting in (x, Q^2) on the Hall C experimental results web page [44]. In this table, each HMS spectrometer setting was divided in two, with relative scattering angle either positive or negative. A total of 20,000 bins are listed, based on the criterion that the Monte Carlo simulation prediction was for more than 4 counts, to ensure approximately Gaussian statistical errors on the experimental data. The table also includes results from thirteen additional HMS settings taken in Fall 2018 and Spring 2019 to study charge-symmetry violation in pion fragmentation functions, as reported in Ref. [29]. These settings covered a small range $\langle P_t \rangle \sim 0.1$ GeV, and therefore are not included in the results of the present publication. The tables also include multiplicity results with no radiative corrections applied, which may prove useful in future global fits with consistent radiative correction models and formalism.

B. Pion multiplicities as a function of (z, P_t, ϕ^*)

The ϕ^* dependence of the semi-inclusive pion electroproduction multiplicity $M(x, Q^2, z, P_t, \phi^*)$ is shown in discrete bins of z and P_t for kinematic setting I ($x = 0.31$, $Q^2 = 3.1$ GeV 2 , $W = 2.8$ GeV) in Fig. 9. For clarity, adjacent bins in z were combined together, and only eight bins in P_t are shown; at higher values of P_t , the ϕ^* coverage becomes increasingly

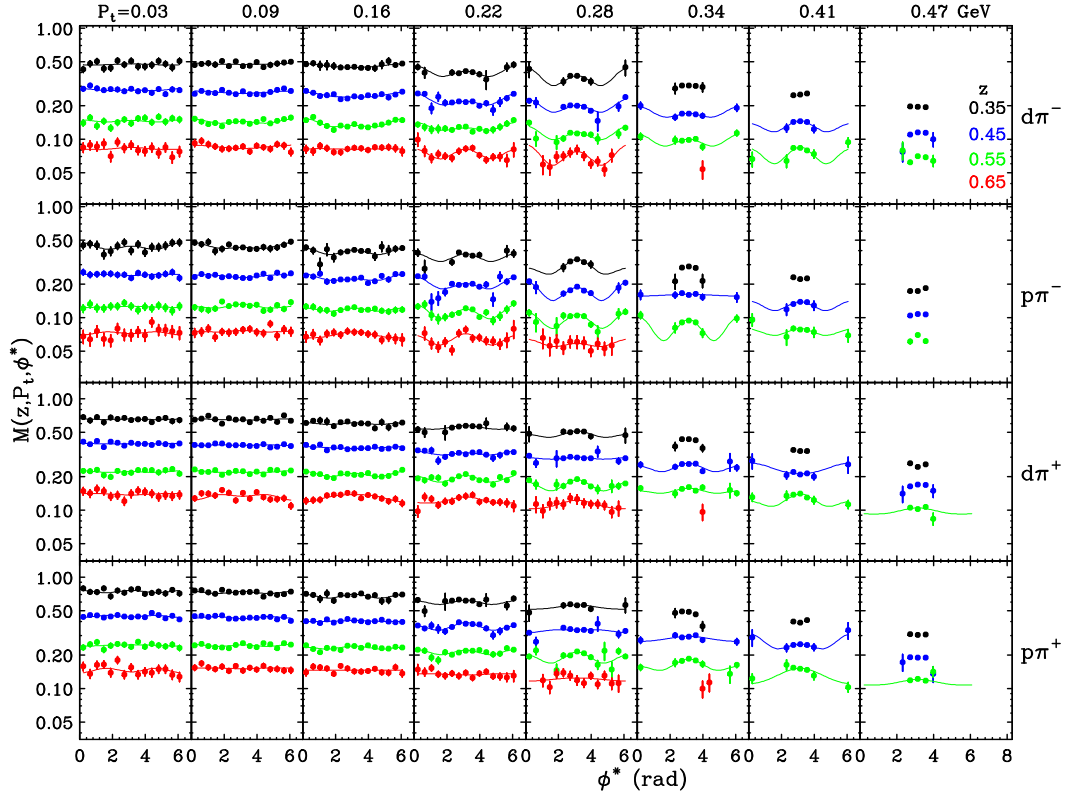


FIG. 9. Pion multiplicity as a function of ϕ^* for $x = 0.31$, $Q^2 = 3$ GeV 2 (kinematic setting I) for eight bins in P_t (left to right) and four target/final-state configurations (top to bottom), for four values of z as indicated on the right edge of the rightmost panels. Relative systematic errors (not shown) are estimated to be 2.2% point-to-point and 1.8% for the scale uncertainty. The solid curves are fits to each dataset at fixed z , P_t , target, and pion charge with the functional form $M_0[1 + A \cos(\phi^*) + B \cos(2\phi^*)]$. No fully differential results from previously published experiments are available to compare to.

centered near 180 degrees due to the use of in-plane spectrometers in this experiment. Similarly, the results for settings II and III are shown in Fig. 10 and Fig. 11 respectively.

The main features of the data are:

- the multiplicity decreases with increasing z ;
- the multiplicity decreases with increasing P_t ; and
- the distributions tend to be mostly independent of ϕ^* at fixed values of z and P_t .

To quantify this behavior, each dataset at fixed z , P_t , target, and pion charge was fit

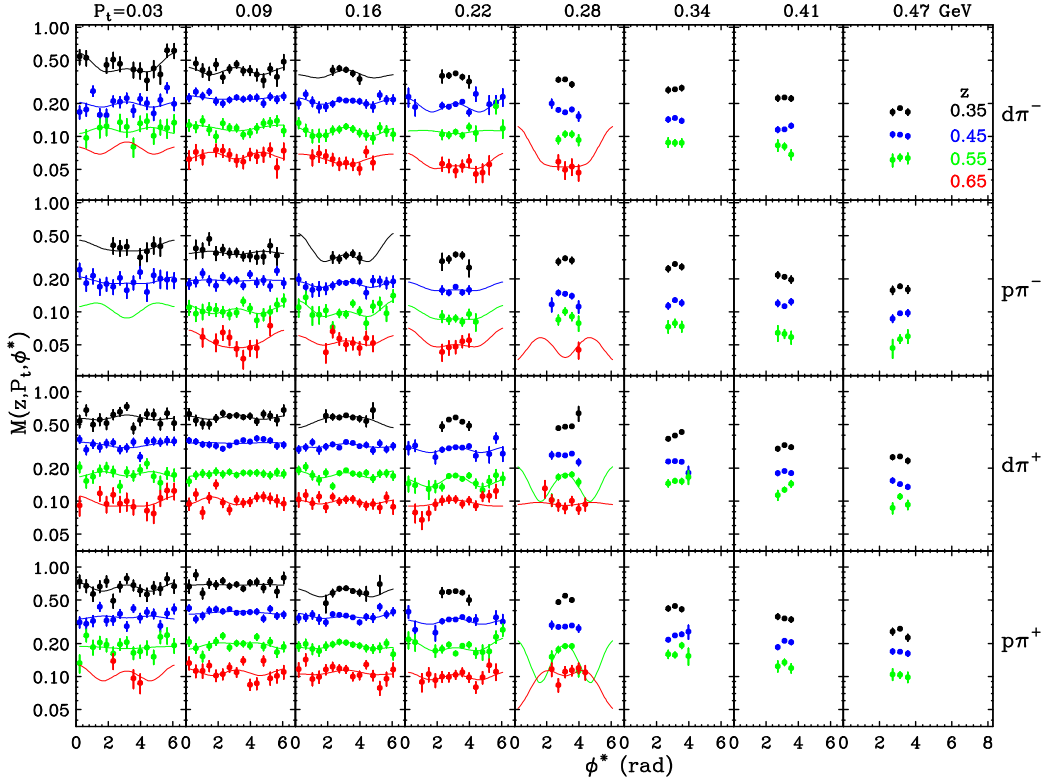


FIG. 10. Pion multiplicity as a function of ϕ^* for $x = 0.30$, $Q^2 = 4.1$ GeV 2 (kinematic setting II) for eight bins in P_t (left to right) and four target/final-state configurations (top to bottom), for four values of z as indicated on the right edge of the rightmost panels. Relative systematic errors (not shown) are estimated to 2.2% point-to-point and 1.8% for the scale uncertainty. The solid curves are fits to each dataset at fixed z , P_t , target, and pion charge with the functional form $M_0[1 + A \cos(\phi^*) + B \cos(2\phi^*)]$. No fully differential results from previously published experiments are available to compare to.

with the functional form

$$M_0[1 + A \cos(\phi^*) + B \cos(2\phi^*)]. \quad (10)$$

In terms of the standard structure functions [3],

$$M_0 = (F_{UU,T} + \epsilon F_{UU,L}) / (F_T + \epsilon F_L)$$

$$A = \sqrt{2\epsilon(1 + P_t)} F_{UU}^{\cos(\phi^*)} / (F_{UU,T} + \epsilon F_{UU,L})$$

$$B = P_t F_{UU}^{\cos(2\phi^*)} / (F_{UU,T} + \epsilon F_{UU,L})$$

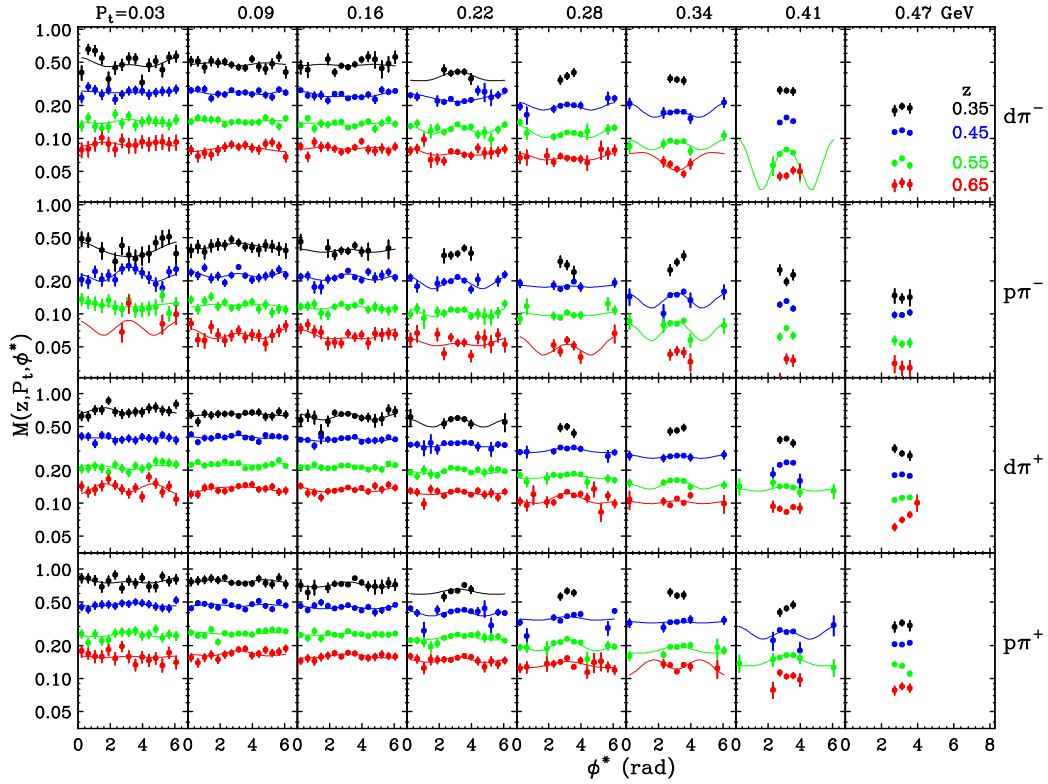


FIG. 11. Pion multiplicity as a function of ϕ^* for $x = 0.45$, $Q^2 = 4.5 \text{ GeV}^2$ (kinematic setting III) for eight bins in P_t (left to right) and four target/final-state configurations (top to bottom), for four values of z as indicated on the right edge of the rightmost panels. Relative systematic errors (not shown) are estimated to be 1.3% point-to-point and 1.8% for the scale uncertainty. The solid curves are fits to each dataset at fixed z , P_t , target, and pion charge with the functional form $M_0[1 + A \cos(\phi^*) + B \cos(2\phi^*)]$. No fully differential results from previously published experiments are available to compare to.

The fit results are discussed in the next subsections.

C. Pion multiplicities averaged over ϕ^*

The results for the ϕ^* averaged parameter, M_0 , from the fits described above are displayed in Fig. 12 as a function of P_t for the three kinematic settings, the target and pion charge combinations, in four bins in z . The measured multiplicities are compared to the calculation

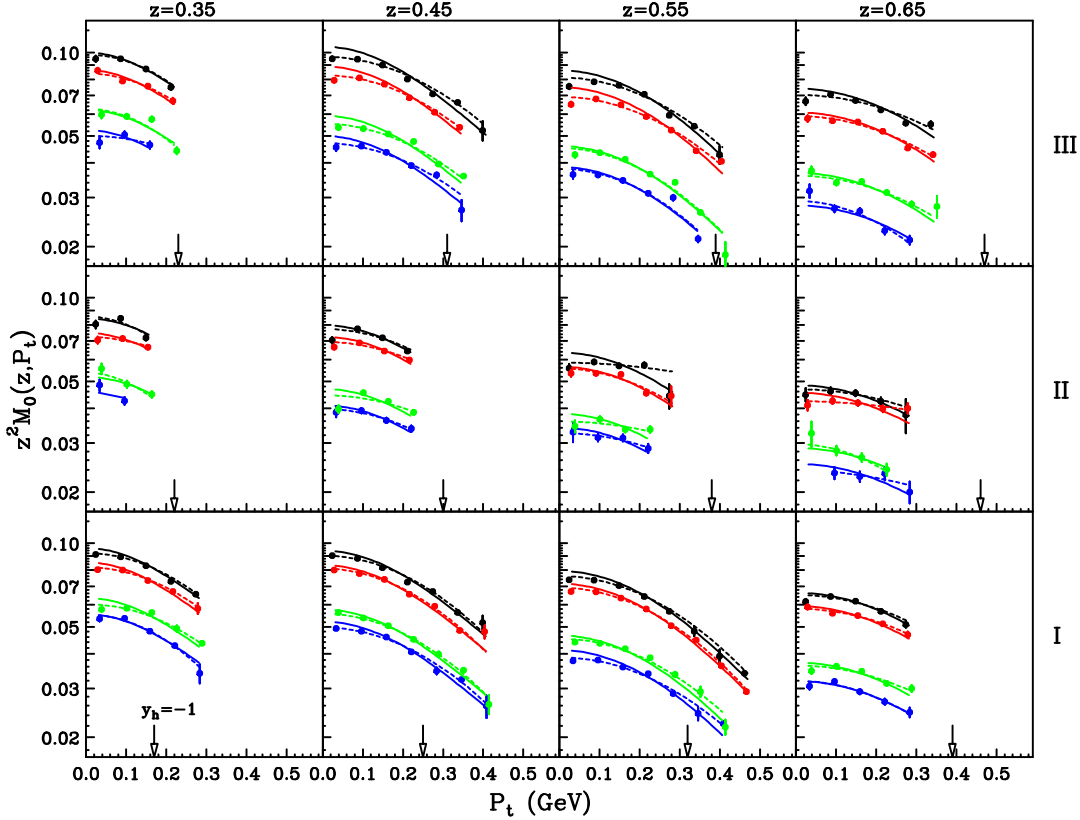


FIG. 12. The ϕ^* averaged fit parameter M_0 weighted by z^2 , as a function of P_t , for the three kinematic settings of this experiment (top to bottom) in four bins in z (left to right). Within each panel, the results from top to bottom are for π^+ from a proton target (black), π^+ from a deuteron target (red), π^- from a deuteron target (green) and π^- from a proton target (blue). Relative systematic errors (not shown) are estimated to be 1.3% (2.2%) point-to-point for setting III (settings I and II) and 1.8% for the scale uncertainty. The curves are the predictions of the MAP collaboration based on a fit to previous world data [28, 45, 46], normalized with a parameter k to give the best overall agreement with these results. The dashed curves illustrate two-parameter Gaussian fits to each dataset of the form $M = ae^{-bP_t^2}$. The arrows point to the values of P_t for which $y_h = -1$, where y_h is the definition of rapidity used in Ref. [47].

of MAP [28, 45, 46] scaled by P_t -independent normalization factors k that give the best agreement with these data. The MAP calculations, which use a combination of Gaussian and weighted Gaussian distributions in P_t , based on a fit to data from HERMES and COMPASS, are generally in good agreement with the measured P_t -dependence. Also shown in Fig. 12 are

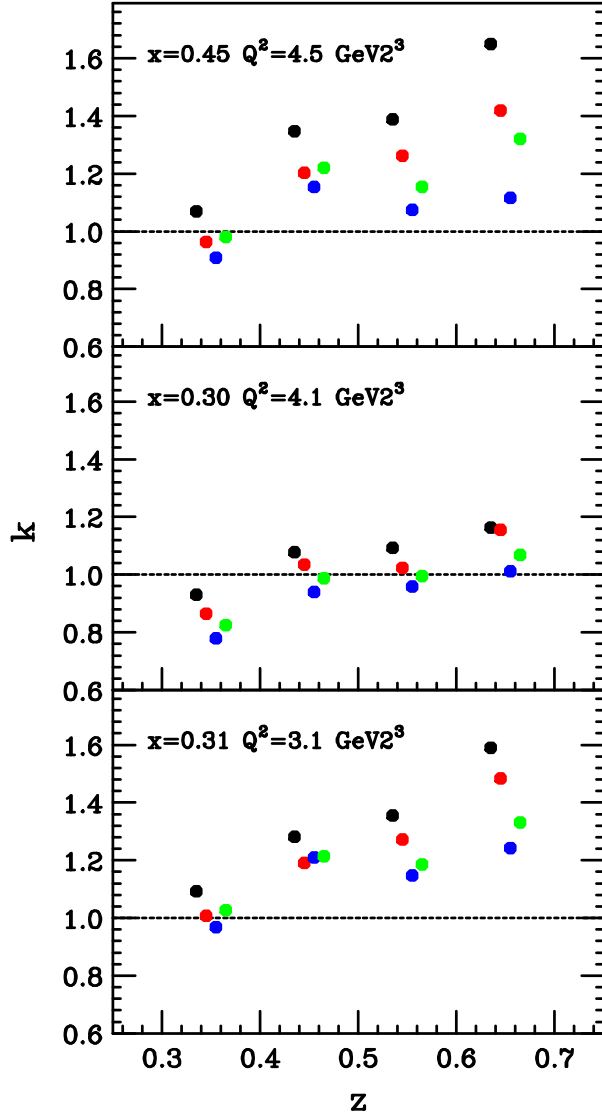


FIG. 13. Normalization factors k that best match our results and the MAP calculations [28, 45, 46] for the three kinematic settings of this experiment (top to bottom), as a function of z , and the four flavor cases (color scheme same as in Fig. 12).

Gaussian fits of the form $ae^{-bP_t^2}$. It can be seen that the fits are roughly parallel to each other when plotted on a logarithmic scale, indicating only small differences in the slope parameters b . In the simple ansatz that $b^{-1} = \langle \vec{p}_\perp^2 \rangle + z^2 \langle \vec{k}_T^2 \rangle$, this implies small differences in $\langle \vec{k}_T^2 \rangle$ for up and down quarks, as well as small difference in the widths of favored fragmentation and unfavored fragmentation functions. This is discussed further in the next section.

The P_t -independent normalization factors k are plotted in Fig. 13 as a function of z , for

the target and pion charge combinations and the three kinematic settings. They are, on average, closest to unity for setting II ($W = 3.3$ GeV), and tend to be larger than unity for setting I ($W = 2.8$ GeV), and even larger for setting III ($W = 2.6$ GeV). There is also a clear trend for k to increase with increasing z , especially for positive pions from the proton target, and to a lesser extent for the positive pions from the deuteron target. These trends are likely related to the fact that the present data are at lower W and higher x than the HERMES and COMPASS data that went into the MAP global fit.

D. Pion multiplicities near $\phi^* = 180^\circ$

Due to the experimental setup limitations, it was not possible to obtain full azimuthal coverage at large P_t . Nonetheless, a considerable amount of time was spent accumulating data near $\phi^* = 180^\circ$, which primarily measures $M_0(1 - A + B)$. Given this caveat, it is of interest to plot the multiplicities at $\langle\phi^*\rangle \sim 180^\circ$, over the full P_t experimental range, as shown in Fig. 14. The MAP calculations for M_0 (MAP did not include non-zero values of A and B in their fits) describe the P_t -independence quite well up to $P_t = 0.5$ GeV, which is the largest value provided by the collaboration. Although not perfect in magnitude, the Gaussian-shaped fits shown in the figure describe the P_t -independence remarkably well to values of P_t as high as 0.7 GeV.

The slope parameters b for the above fits are displayed in Fig. 15 as a function of z . The values decrease with increasing z , with a rough global fit to all three kinematic settings given by $b = (0.185 + z^2 0.28)^{-1}$ GeV $^{-2}$. With the simple ansatz $b^{-1} = \langle\vec{p}_\perp^2\rangle + z^2 \langle\vec{k}_T^2\rangle$, the up and down quark widths $\langle\vec{k}_T^2\rangle \sim 0.28$ GeV $^{-2}$ and the fragmentation widths $\langle\vec{p}_\perp^2\rangle \sim 0.185$ GeV $^{-2}$. As mentioned in the previous section, this is consistent with little or no differences in $\langle\vec{k}_T^2\rangle$ for up and down quarks, as well as the widths of favored and unfavored fragmentation functions.

To further quantify the observed flavor independence of the multiplicities, the ratio of $\langle\phi^*\rangle \sim 180^\circ$ multiplicities for (d, π^+) , (p, π^-) , and (d, π^-) to the multiplicities for (p, π^+) are plotted in Fig. 16, as a function of P_t for the three kinematic settings and four z bins. The ratios are consistent with no statistically significant dependence on P_t . The ratios are compared to those from the MAP calculations [28, 45, 46], which also show only very slight P_t -dependence.

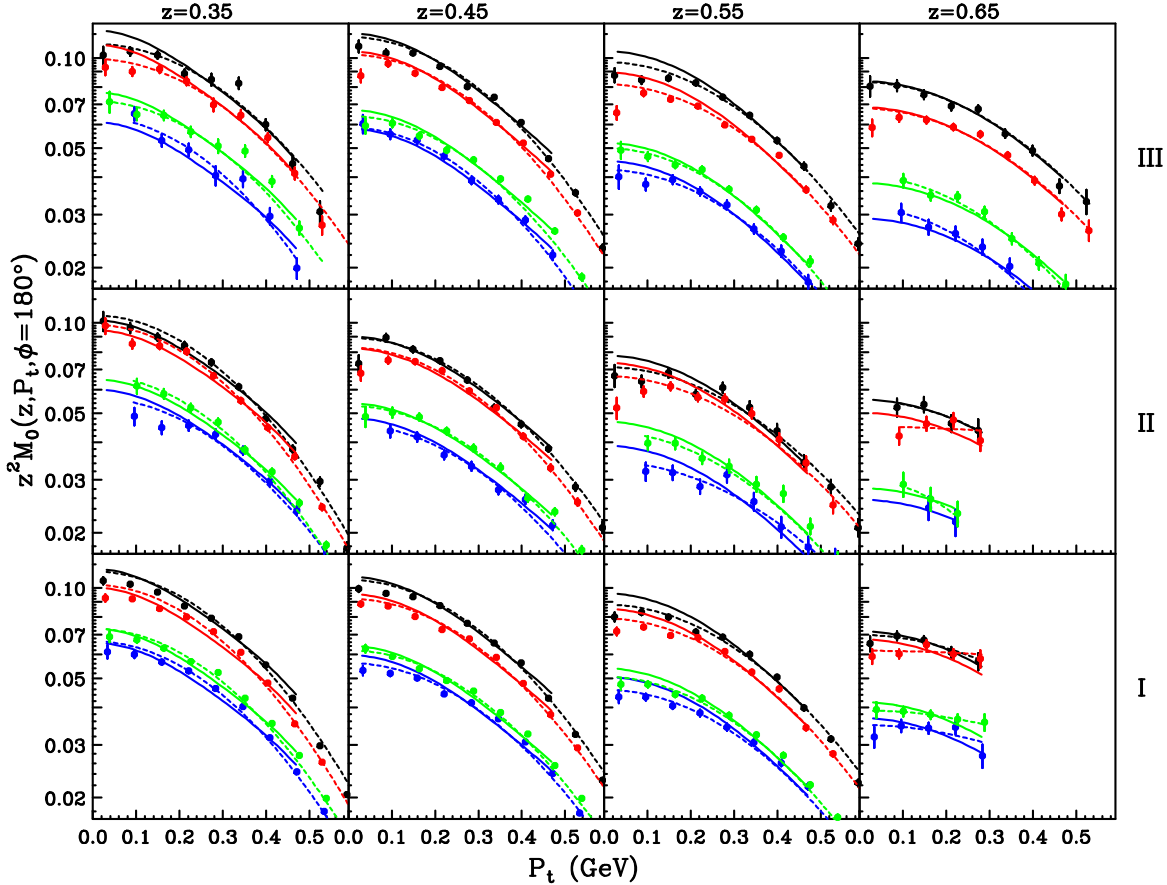


FIG. 14. The fit parameter M_0 weighted by z^2 as a function of P_t , averaged over $150 < \phi^* < 210$ degrees, for the three kinematic settings of this experiment (top to bottom) in four bins in z (left to right). Within each panel, the results from top to bottom are for π^+ from a proton target (black), π^+ from a deuteron target (red), π^- from a deuteron target (green) and π^- from a proton target (blue). Relative systematic errors (not shown) are estimated to be 1.3% (2.2%) point-to-point for setting III (settings I and II) and 1.8% for the scale uncertainty. The curves are the predictions of the MAP collaboration based on a fit to previous world data [28, 45, 46], normalized with a parameter k to give the best overall agreement with these results. The dashed curves illustrate two-parameter Gaussian fits to each dataset of the form $M = ae^{-bP_t^2}$. No fully differential results from previously published experiments are available for comparison.

E. Azimuthal dependence of multiplicities

The ϕ^* dependence of the measured multiplicities is quantified by the two coefficients, A and B , associated with the $\cos(\phi^*)$ and $\cos(2\phi^*)$ modulations of the multiplicities. The

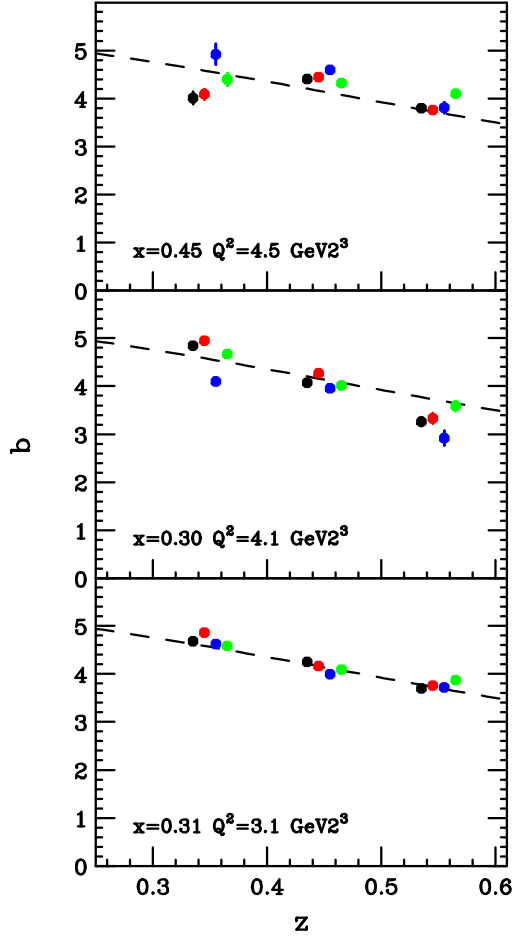


FIG. 15. Slope parameters b for the fits shown Fig. 14 as a function of z for the three kinematic settings of this experiment (top to bottom) and the four flavor cases (color scheme same as in Fig. 12).

$\cos(\phi^*)$ coefficient, A , obtained from the fit of the multiplicity results in each (z, P_t) bin to functional form—Eq. 10, is shown in Fig. 17 as a function of P_t . These results show an overall trend that A for π^- production on both protons and deuterons is significantly > 0 at high z for all three kinematic settings. On the other hand, the A coefficient is consistent with zero within experimental uncertainties or has small negative values for π^+ production on both protons and deuterons. The π^+ results are consistent with the previous HERMES measurements [23] but have the opposite sign for the π^- , except for the HERMES point [23] at highest x . We note that all of these data generally lie at higher x than those from HERMES [23] or COMPASS [26]. Similarly the $\cos(2\phi^*)$ coefficient, B , obtained from the fit of the multiplicity results in each (z, P_t) bin to Eq. 10 is shown in Fig. 18 as a function

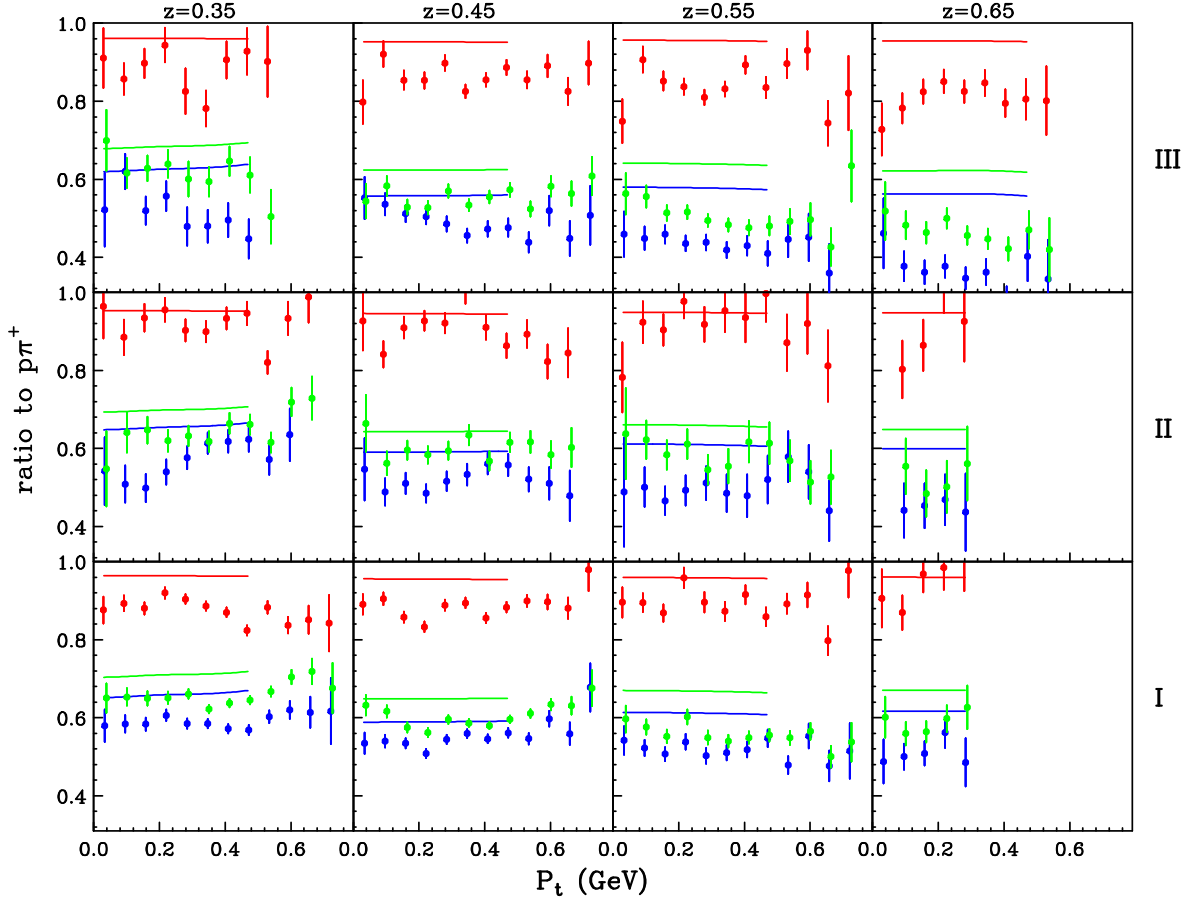


FIG. 16. Ratios to (p, π^+) of experimental multiplicities averaged over $150^\circ < \phi^* < 210^\circ$ degrees for (d, π^+) (red), (p, π^-) (green), and (d, π^-) (blue). Systematic errors (not shown) are discussed in the text. The solid curves are the ratios of MAP calculations, while the dashed curves are the ratios of Gaussian fits from Fig. 14. The curves follow the same color scheme as the data points.

of P_t . Other than a couple of z bins, these results show small values of B , that are either consistent with zero or have small positive values. These results are consistent with the previous HERMES measurements [23] except at $\langle z \rangle = 0.55$.

V. SYSTEMATIC UNCERTAINTIES AND CAVEATS

A. Experimental systematic studies

The entire analysis was performed with several alternative sets of cuts and PID criteria. One study used a smaller range in track momenta and angles. Another ignored the heavy

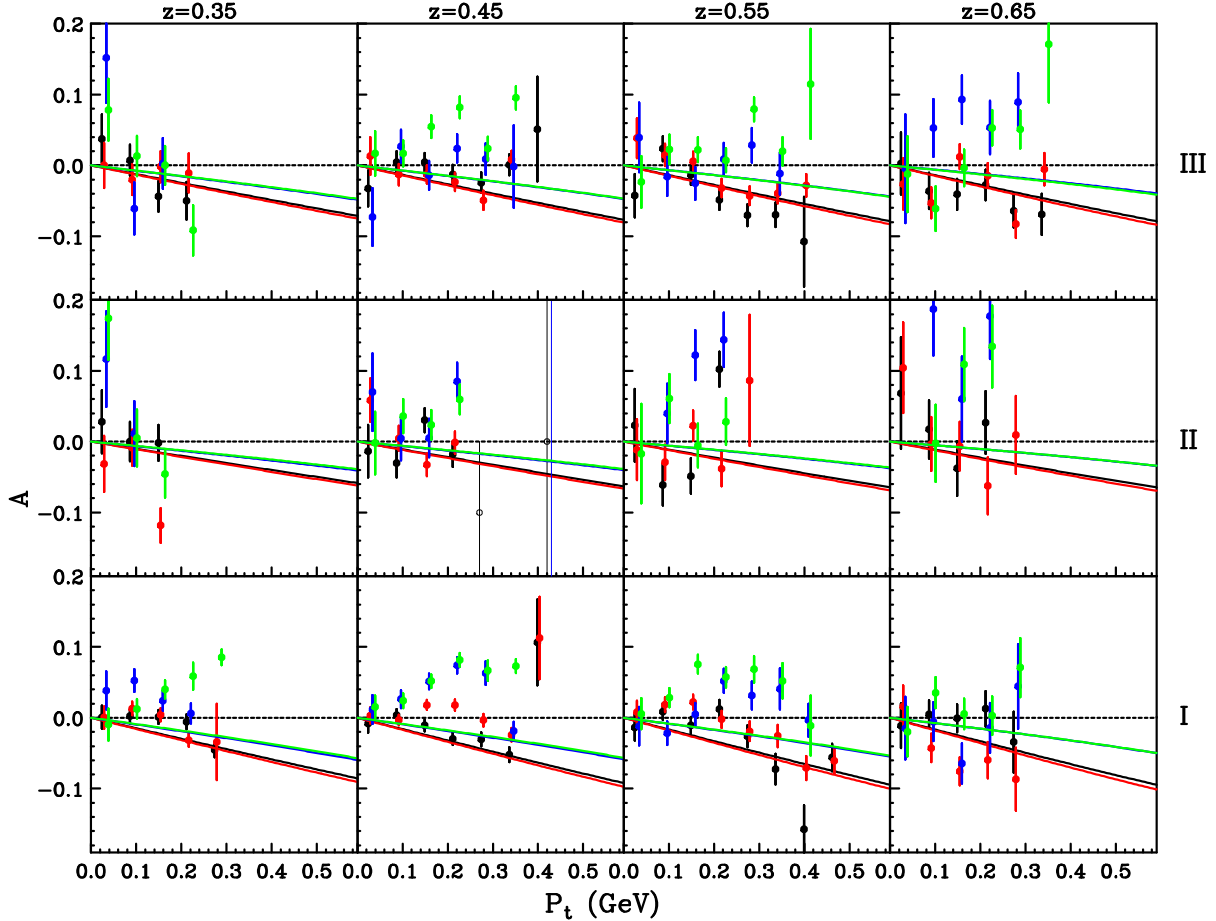


FIG. 17. Results from this experiment (solid circles) for the coefficients A that scale the $\cos(\phi^*)$ distributions for (p, π^+) (black), (d, π^+) (red), (p, π^-) (green), and (d, π^-) (blue). Relative systematic errors (not shown) are estimated to be 0.01 (0.02) point-to-point for setting III (settings I and II). The scale uncertainty is negligibly small. The open circles are from HERMES at $Q^2 = 6.6$ GeV 2 , $x = 0.36$ and $\langle z \rangle = 0.45$ [16], and curves are from a fit to HERMES and COMPASS data [16, 23]. The curves follow the same color scheme as the data points.

gas Cherenkov detector in the SHMS, which resulted in significant kaon contamination of the pion sample above momenta of 3 GeV. A third study used a lower aerogel threshold, with correspondingly larger kaon contamination subtraction. The luminosity and HMS acceptance were verified to be accurate to within 3% by comparison of elastic electron-proton measurements to a fit to global data [40]. The optical properties of the spectrometers were verified using the kinematic constraints of both ep elastic scattering and exclusive pion production.

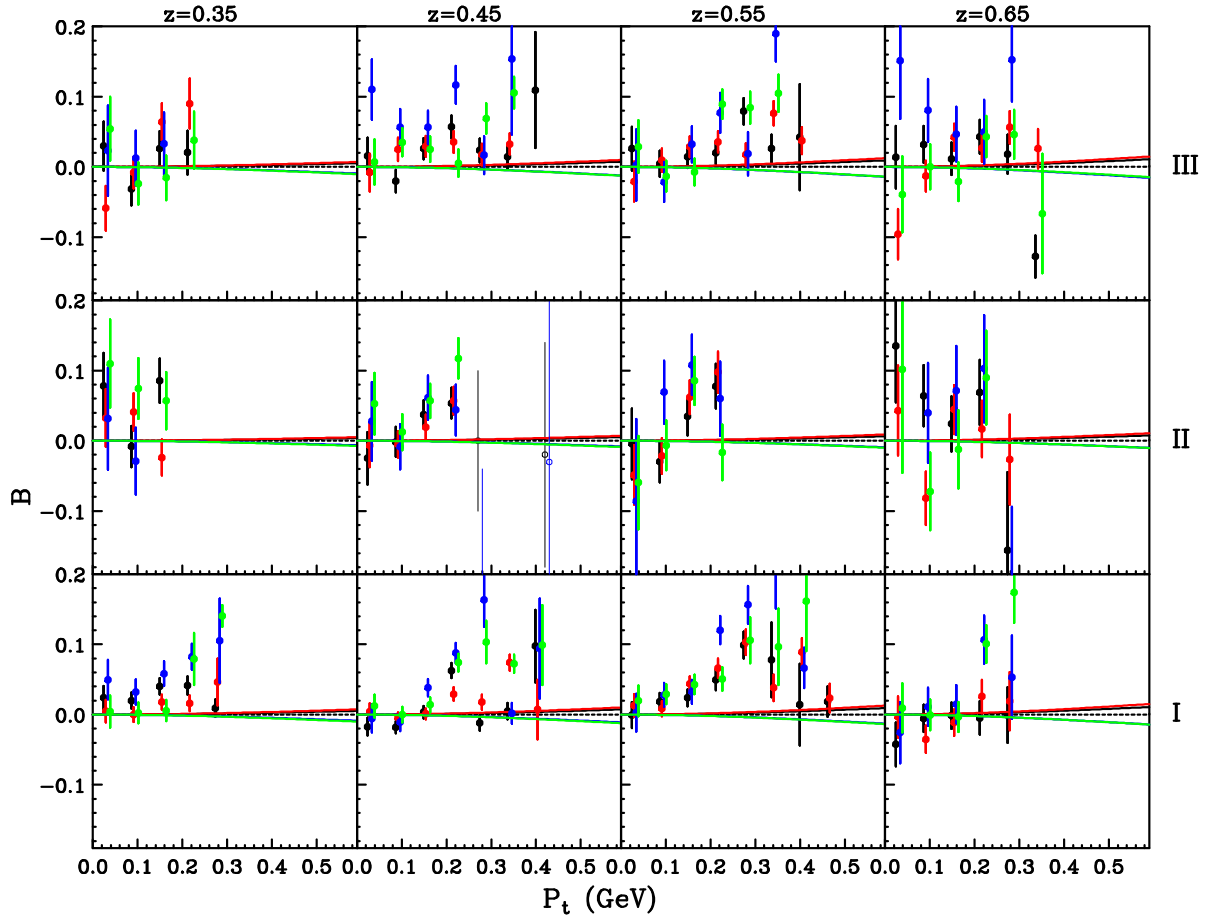


FIG. 18. Results from this experiment (solid circles) for the coefficients B that scale the $\cos(2\phi^*)$ distributions for (p, π^+) (black), (d, π^+) (red), (p, π^-) (green), and (d, π^-) (blue). Relative systematic errors (not shown) are estimated to be 0.01 (0.02) point-to-point for setting III (settings I and II). The scale uncertainty is negligibly small. The open circles are from HERMES at $Q^2 = 6.6 \text{ GeV}^2$, $x=0.36$ and $\langle z \rangle = 0.45$ [16], and curves are from a fit to HERMES and COMPASS data [16, 23]. The curves follow the same color scheme as the data points.

B. Experimental systematic errors

The main sources of systematic uncertainties are listed in Table VI, based on the studies mentioned above as well as known instrumental uncertainties. They have been divided into two categories: normalization/scale uncertainties that impact all measurements on a given target equally, and point-to-point uncertainties that vary with pion kinematics and charge. The overall experimental systematic error is estimated to be about 2.5% for setting III. Due

to many problems in Spring 2018, we estimate an additional overall normalization error of 2% for settings I and II.

In ratios of π^+/π^- , most systematic errors cancel out except for the uncertainty in particle identification. In ratios of proton to deuteron target for a fixed flavor, most systematic errors cancel except for the relative target thickness.

TABLE VI. Principal experimental systematic uncertainties, divided in overall normalization (scale) uncertainties and those that vary with pion kinematics.

Source	Scale	Point-to-Point
	Uncertainty (%)	Uncertainty (%)
Charge	-	0.5
Target density	1	-
Target boiling correction	-	0.3
Target end cap subtraction	0.3	-
Particle identification	1	-
PID Purity	-	0.2
Spectrometer Acceptance	1	0.5
Kinematics	-	0.3
Rate dependence	-	1-2
Total	1.8	1.3-2.2

C. Radiative corrections uncertainty

The application of radiative corrections is ideally an iterative process in which all available global data are iteratively analyzed until convergence is achieved. For the present analysis, we rely on our fits to the world data (including our own) on three physics processes: exclusive pion production, Δ resonance production, and ρ meson production. Our fit to exclusive pion production is driven largely by preliminary, unpublished results from Hall C experiments conducted between 2018 and 2022. The combined statistical and systematic error on the fit is of the order 5% for π^+ and 10% for π^- (applicable only for the deuteron target). Since the radiative tail from exclusive pion production varies from 1% to 10%, we estimate

a model uncertainty of $0.1 - 0.5\%$ ($0.2 - 1\%$) for the exclusive pion radiative tails to π^+ (π^-) production. Due to lack of available data, our simple fit to $\pi\Delta$ production is much less certain, resulting in a range of $0.5 - 3\%$ uncertainty, depending on pion kinematics. The ratio of radiated to unradiated SIDIS cross sections is relatively insensitive to the absolute normalization of the model and is primarily driven by the kinematic dependence on z and P_t . Based on our iterations of the model, we estimate about 1% uncertainty in the radiative corrections due to the SIDIS model, roughly independent of pion kinematics.

Other sources of radiative correction uncertainty could arise from the use of the angle-peaking approximation (photons emitted only along the incident or scattered electron direction), the uncertainty in the soft-photon term, use of the equivalent radiator approximation, the neglect of pion radiation, and the lack of two-photon corrections.

We have listed our results [44] both with and without radiative corrections, so that future global analyses can improve on the cross section models by incorporating data in kinematic regions not constrained by the present experiment, as has been done previously for DIS data.

D. Relevance to TMD factorization

The authors of Ref. [47] have presented three kinematic regions for pion electroproduction: the target fragmentation region; a soft central region; and a current fragmentation region where TMD factorization should be applicable. They postulate that the probability of the current fragmentation region dominating by more than 2σ requires that the hadron rapidity $y_h < -1$, corresponding to the regions to the left of the arrows in Fig. 12. Most of the present data lie in this region.

Some previous experiments [23, 48] have subtracted contributions from pions originating from diffractive ρ electroproduction, a process that is clearly not easily accounted for in the TMD factorization framework. Due to a lack of experimental data in our kinematic region, we have not corrected our results for the contributions from diffractive vector meson production. Based on an extrapolation of the COMPASS collaboration fit [48], there could be substantial corrections to the $\langle \cos(\phi^*) \rangle$ and $\langle \cos(2\phi^*) \rangle$ moments, but small corrections for $x > 0.1$, where all of the present data lie.

The data presented in this paper were taken at a single beam energy, and thus cannot be used to separate the transverse and longitudinal structure functions.

VI. SUMMARY

In summary, we have measured the π^\pm multiplicities from SIDIS on H and D targets over a three-dimensional grid in z , P_t , and ϕ^* for several values of (x, Q^2) . The multiplicities were fitted for each bin in (x, Q^2, z, P_t) with three parameters: ϕ^* -independent M_0 , and azimuthal modulations $\langle \cos(\phi^*) \rangle$ and $\langle \cos(2\phi^*) \rangle$. The P_t -dependence of the M_0 results was found to be remarkably consistent for the four flavor cases studied: $ep \rightarrow e\pi^+X$, $ep \rightarrow e\pi^-X$, $ed \rightarrow e\pi^+X$, $ed \rightarrow e\pi^-X$ over the range $0 < P_t < 0.4$ GeV, as were the multiplicities evaluated near $\phi^* = 180^\circ$ over the extended range $0 < P_t < 0.7$ GeV. Gaussian widths of the P_t -dependence exhibit a quadratic increase with z . The $\cos(\phi^*)$ modulations were found to be consistent with zero for π^+ , in agreement with previous world data, while the π^- moments were in many cases significantly greater than zero. The $\cos(2\phi^*)$ modulations were found to be consistent with zero. The higher statistical precision of this dataset compared to previously published data should allow improved determinations of quark transverse momentum distributions and higher twist contributions.

The spin-averaged SIDIS results of this paper are but one part of a larger program at JLab, which includes the use of nuclear targets, polarized beams and targets, and a range of beam energies to separate longitudinal and transverse structure functions.

VII. ACKNOWLEDGMENTS

We are grateful to M. Cerutti for providing calculations of the 2022 MAP model at each of the kinematic settings of this experiment

This work was funded in part by the U.S. Department of Energy, including contract AC05-06OR23177 under which Jefferson Science Associates, LLC operates Thomas Jefferson National Accelerator Facility, and by the U.S. Department of Energy, Office of Science, contract numbers DE-AC02-06CH11357, DE-FG02-07ER41528, DE-FG02-96ER41003, and by the U.S. National Science Foundation grants PHY 2309976, 2012430, 2013002 and 1714133 and the Natural Sciences and Engineering Research Council of Canada grant SAPIN-2021-00026. We wish to thank the staff of Jefferson Lab for their vital support throughout the experiment. We are also grateful to all granting agencies providing funding support to the authors throughout this project.

- [1] M. Anselmino, M. Boglione, U. D'Alesio, A. Kotzinian, F. Murgia, and A. Prokudin, Phys. Rev. D **71**, 074006 (2005).
- [2] M. Anselmino, A. Efremov, A. Kotzinian, and B. Parsamyan, Phys. Rev. D **74**, 074015 (2006).
- [3] A. Bacchetta, M. Diehl, K. Goeke, A. Metz, P. Mulders, and M. Schlegel, J. High Energy Phys. **02**, 093 (2007).
- [4] R. P. Feynman, Phys. Rev. Lett. **23**, 1415 (1969).
- [5] P. Mulders and R. Tangerman, Nucl. Phys. B **461**, 197 (1996).
- [6] D. Boer, P. J. Mulders, and O. V. Teryaev, Phys. Rev. D **57**, 3057 (1998), arXiv:hep-ph/9710223.
- [7] X. Ji, J.-P. Ma, and F. Yuan, Phys. Lett. B **597**, 299 (2004).
- [8] T. Navasardyan *et al.*, Phys. Rev. Lett. **98**, 022001 (2007).
- [9] H. Mkrtchyan, P. E. Bosted, *et al.*, Phys. Lett. B **665**, 20 (2008).
- [10] M. Osikenki *et al.*, Phys. Rev. D **80**, 032004 (2009).
- [11] R. Asaturyan *et al.*, Phys. Rev. C **85**, 015202 (2012).
- [12] M. Anselmino *et al.*, Eur. Phys. J. A **47**, 35 (2011).
- [13] V. Barone, F. Bradamante, and M. A., Prog. Part. Nucl. Phys **65**, 267 (2010).
- [14] A. Bacchetta and M. Radici, Phys. Rev. Lett. **107**, 212001 (2011).
- [15] M. Anselmino, M. Boglione, J. O. Gonzalez-Hernandez, S. Melis, and A. Prokudin, J. High Energy Phys. **04**, 005 (2014).
- [16] V. Barone, M. Boglione, J. O. Gonzalez Hernandez, and S. Melis, Phys. Rev. D **91**, 074019 (2015).
- [17] A. Bacchetta, F. Delcarro, C. Pisano, M. Radici, and A. Signori, J. High Energy Phys. **06**, 81 (2017).
- [18] R. N. Cahn, Phys. Lett. B **78**, 269 (1978).
- [19] D. Boer and P. J. Mulders, Phys. Rev. D **57**, 5780 (1998).
- [20] J. Collins, Nuclear Physics B **396**, 161 (1993).
- [21] C. J. Bebek, C. N. Brown, M. Herzlinger, S. D. Holmes, C. A. Lichtenstein, F. M. Pipkin, S. Raither, and L. K. Sisterson, Phys. Rev. Lett. **34**, 759 (1975).

- [22] A. Airapetian *et al.* (HERMES), Phys. Rev. D **87**, 074029 (2013), arXiv:1212.5407 [hep-ex].
- [23] A. Airapetian *et al.* (HERMES), Phys. Rev. D **87**, 012010 (2013), arXiv:1204.4161 [hep-ex].
- [24] J. Ashman *et al.* (EMC), Z. Phys. C 52 (1991) 361-388 **52**, 361 (1991).
- [25] G. D. Alexeev *et al.* (COMPASS), Phys. Rev. D **112**, 012002 (2025), arXiv:2410.12005 [hep-ex].
- [26] C. Adolph *et al.* (COMPASS), Eur.Phys.J.C **73**, (2013) 8, 2531, erratum Eur.Phys.J.C 75 (2015) 2, 94, arXiv:1305.7317 [hep-ex].
- [27] V. Benešová (COMPASS), PoS **DIS2024**, 223 (2025), arXiv:2407.14669 [hep-ex].
- [28] A. Bacchetta, V. Bertone, C. Bissolotti, G. Bozzi, M. Cerutti, F. Delcarro, M. Radici, L. Rossi, and A. Signori (MAP), JHEP **08**, 232 (2024), arXiv:2405.13833 [hep-ph].
- [29] H. Bhatt *et al.*, Phys. Lett. B **865**, 139485 (2025), arXiv:2408.16640 [nucl-ex].
- [30] S. Ali et al., arXiv:2503.08706 [physics.ins-det], <https://arxiv.org/pdf/2503.08706.pdf>, submitted to Nucl. Inst. and Meth.
- [31] SURA-CEBAF, *CEBAF Conceptual Design Report: Basic Experimental Equipment*, Tech. Rep. (SURA-CEBAF, Newport News, Virginia, 1990) university of North Texas Libraries, UNT Digital Library.
- [32] H. Mkrtchyan *et al.*, Nuclear Instruments and Methods in Physics Research Section A: Accelerators, Spectrometers, Detectors and Associated Equipment **719**, 85 (2013).
- [33] CLAS Collaboration, Jefferson Lab., <https://www.jlab.org/physics/hall-b/clas>.
- [34] CLAS12 Collaboration, Jefferson Lab., <https://www.jlab.org/physics/hall-b/clas12>.
- [35] H. Bhatt, PhD Dissertation, Mississippi State University, 2024. <https://misportal.jlab.org/sti/publications/23431>.
- [36] S. Jia, PhD Dissertation, Temple University, 2022. <https://misportal.jlab.org/sti/publications/21868>.
- [37] CEBAF Data Acquisition System (DAQ), <https://coda.jlab.org>.
- [38] Hall C MC, https://hallcweb.jlab.org/wiki/index.php/SIMC_Monte_Carlo and https://github.com/JeffersonLab/simc_gfortran.
- [39] L. W. Mo and Y. S. Tsai, Rev. Mod. Phys. **41**, 205 (1969).
- [40] P. E. Bosted and M. E. Christy, Phys. Rev. C **77**, 065206 (2008).
- [41] S. Kuhlmann, Nuclear Physics B - Proceedings Supplements **79**, 108 (1999), proceedings of the 7th International Workshop on Deep Inelastic Scattering and QCD.

- [42] I. Schienbein, V. A. Radescu, G. P. Zeller, M. E. Christy, C. E. Keppel, K. S. McFarland, W. Melnitchouk, F. I. Olness, M. H. Reno, F. Steffens, and J.-Y. Yu, Journal of Physics G: Nuclear and Particle Physics **35**, 053101 (2008).
- [43] T. Horn, PhD Dissertation, University of Maryland, 2006. https://physics.umd.edu/enp/theses/horn_thesis_04-25-06-revised.pdf.
- [44] Hall C pion-SIDIS results , https://hallcweb.jlab.org/experiments/HALLC_SIDIS/.
- [45] A. Bacchetta, V. Bertone, C. Bissolotti, G. Bozzi, M. Cerutti, F. Piacenza, M. Radici, and A. Signori, J. High Energy Phys. **10**, 127 (2022).
- [46] M. Cerutti, Private communications, 2024.
- [47] M. Boglione, M. Diefenthaler, S. Dolan, L. Gamberg, W. Melnitchouk, D. Pitonyak, A. Prokudin, N. Sato, and Z. Scalyer (Jefferson Lab Angular Momentum (JAM)), JHEP **04**, 084 (2022), arXiv:2201.12197 [hep-ph].
- [48] J. Agarwala *et al.* (COMPASS), Nucl. Phys. B **956**, 115039 (2020), arXiv:1912.10322 [hep-ex]